Journal Pre-proof

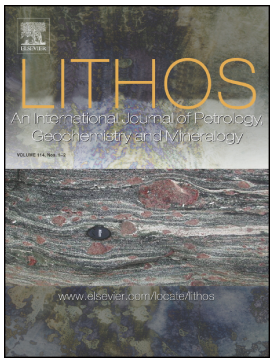

Petrogenesis of the post-collisional rare-metal-bearing Ad-Dayheen granite intrusion, Central Arabian Shield

Bassam A. Abuamarah, Mokhles K. Azer, Paul D. Asimow, Qingshang Shi

PII: S0024-4937(20)30591-0

DOI: https://doi.org/10.1016/j.lithos.2020.105956

Reference: LITHOS 105956

To appear in: *LITHOS*

Received date: 31 October 2020

Revised date: 16 December 2020

Accepted date: 18 December 2020

Please cite this article as: B.A. Abuamarah, M.K. Azer, P.D. Asimow, et al., Petrogenesis of the post-collisional rare-metal-bearing Ad-Dayheen granite intrusion, Central Arabian Shield, *LITHOS* (2020), https://doi.org/10.1016/j.lithos.2020.105956

Petrogenesis of the post-collisional rare-metal-bearing Ad-Dayheen granite intrusion, Central Arabian Shield

Bassam A. Abuamarah[1*], Mokhles K. Azer[2], Paul D. Asimow[3], Qingshang Shi[3,4]

[1] Department of Geology and Geophysics, King Saud University, Riyadh 11451, Saudi Arabia
[2] Geological Sciences Department, National Research Centre,12622-Dokki, Cairo, Egypt
[3] Division of Geological & Planetary Sciences, California Institute of Technology, Pasadena CA 91125, USA
[4] State Key Laboratory of Geological Processes and Mineral Resources, School of Earth Science and Resources, China University of Geosciences Beijing 100083, China

Abstract

At Hadhb't Ad-Dayheen, in the central Arabian Shield, a post-collisional igneous complex called the Ad-Dayheen intrusion is exposed. It was emplaced in the Early Ediacaran (613-625 Ma), during the final tectono-magmatic stage of Arabian Shield development. Despite limited and discontinuous ring-shaped outcrops due to alluvial cover and later faulting, three pulses of intrusion can be recognized in the field: an early pulse of monzogranite; a second pulse of syenogranite and alkali feldspar granite; and a final pulse of alkaline and peralkaline granite, mineralized microgranite, and pegmatite. Samples show distinctively low contents of CaO, MgO, and Sr in contrast to elevated concentrations of alkalis, Rb, Nb, Y, Ta, Hf, Ga, Zr and rare-earth elements (REE); these are common characteristics of post-collisional rare-metal-bearing A-type granites. The suite displays positive Nb-Ta anomalies and pronounced negative Eu anomalies (Eu/Eu* = 0.11-0.35). The alkaline/peralkaline granites and microgranite of the Ad-Dayheen intrusion feature disseminated mineralization, whereas mineralization is localized in the pegmatite. The primary magma feeding the Ad-Dayheen intrusion was mostly generated by partial melting of the juvenile crust of the Arabian Shield, with a minor mantle contribution. We argue that an episode of lithospheric delamination led to crustal uplift, erosional decompression, and generation of mantle melts that supplied heat to drive crustal melting. The anatectic deep crustal melts assimilated a F-bearing component that also added rare metals to the magma. Each

[*] **Corresponding author:** Dr. Bassam A. Abuamarah (Email: babuamarah@ksu.edu.sa)

pulse can be described by a fractional crystallization model, but the parental liquid of each subsequent pulse was first modified by further addition of fluorine and rare metals and loss of CaO, Sr, Ba, and Eu due to fluorite fractionation. Texture and morphology of the ore minerals indicate that mineralization (U, Th, Zr, Nb, Ta, Y, Hf and REE) took place in two stages: a magmatic stage coinciding with emplacement of the intrusion, followed by a hydrothermal stage. The magmatic process enriched the residual melt in high field strength elements (HFSE) and REE. The later hydrothermal stage further localized these elements and increased their concentrations to economic grades. The pegmatite is highly mineralized and contains high concentrations of U (81-179 μg/g), Th (244-600 μg/g), Zr (2397-14927 μg/g), Nb (1352-2047 μg/g), Ta (96-156 μg/g), Y (828-2238 μg/g), Hf (131-377 μg/g) and ∑REE (1969-4761 μg/g).

Keywords: Arabian Shield, Post-collisional Ad-Dayheen intrusion, Rare-metal granite, lithospheric delamination

1. Introduction

The Arabian Shield is the segment of the Arabian–Nubian Shield (ANS) exposed on the Eastern flank of the Red Sea (Hargrove et al., 2006). It developed by terrane accretion during the Neoproterozoic (850–590 Ma) assembly of West and East Gondwana. These terranes are divided by suture zones marked by deformed ultramafic complexes and intruded by various granitoids and mafic-ultramafic plutons (e.g., Genna et al., 2002; Moufti et al., 2013).

The development of the Arabian shield can be divided into pre-collisional, syn-collisional, and post-collisional phases (Johnson and Kattan, 2012). The post-collisional stage (610-590 Ma) involved a transition compressional to extensional tectonics (Genna et al., 2002; Be'eri-Shlevin et al., 2009) and is represented by abundant granitoid intrusions, emplaced at various crustal levels and marked by a range of ages, tectonic settings, and geochemical

characteristics (e.g., Küster, 2009; Ali et al., 2014; Abuamarah, 2020). A number of these post-collisional A-type intrusions take the form of ring complexes (e.g., Harris, 1985; Moghazi et al., 2011; Azer et al., 2014). The post-collisional granitoids of the Arabian Shield are of geodynamic interest (owing to the significant anorogenic addition or reworking of juvenile crustal material) and of economic interest (given their extensive mineralization).

Many A-type granites of the Arabian Shield are marked by significant enrichment of rare metals (e.g., Drysdall and Douch, 1986; Moghazi et al., 2011) and REE (Abuamarah, 2020; Abdullah et al., 2020). Despite several previous studies, the geotectonic evolution and petrogenesis of rare-metal-bearing granites remain controversial. In particular, there has been a long debate on whether the mineralization in these granites is due to magmatic or hydrothermal processes (e.g., Küster, 2009; Abuamarah, 2020). Rare-metal granites are often described as "highly fractionated", implying that concentration of metals to economic levels resulted from passive enrichment in residual melt (e.g., Küster, 2009; Abdallah et al., 2020). However, quantitative fractionation models relating mass removal and degree of enrichment are rarely applied. It remains challenging to explain the progressive depletion of CaO, Sr, Ba, and Eu in these granitoid suites, when plagioclase is typically rare or absent.

The ring complex at Hadhb't Ad-Dayheen (also Hadb Adh-Dayheen), referred to herein as the Ad-Dayheen intrusion, is a good example of a post-collisional rare-metal-bearing granite. Previous studies of its whole-rock geochemistry and geochronology (Moghazi et al., 2011; Ali et al., 2014) did not report mineral chemistry or document the presence or styles of mineralization. This work presents field relations, mineral chemistry, and whole-rock geochemistry of the intrusion and its mineralized zones, in order to shed light on its magmatic sources, petrogenesis, and alteration. We model the fractionation process and discriminate between the products of the

magmatic and hydrothermal stages of mineralization. Finally, we discuss the evolution of the juvenile continental crust of the ANS in light of these results.

2. Geologic setting and field evidence

The ANS consists of a collage of amalgamated ophiolite sequences and associated volcanic arcs that were subsequently modified by widespread plutonic and volcanic activity (e.g., Genna et al., 2002; Azer et al. 2019; Seddik et al., 2020). The abundance of post-collisional anorogenic alkaline/peralkaline plutons and ring complexes is one the most striking features of the northern and western Arabian Shield (Fig. 1). These post-collisional granitoids were often shallowly emplaced and occur both as small oval to sub-circular intrusions (<10 km^2) and as large plutons and batholiths (e.g., Drysdall and Douch, 1986; Küster, 2009; Moghazi et al., 2011; Abuamarah, 2020; Abdallah et al., 2020).

The ring complexes formed by successive intrusion of ring-dikes, cone sheets, plugs and diapirs; they are often associated with extensional structures (Shang et al., 2010). The Ad-Dayheen intrusion is one of the youngest of these complexes. Tectonically, it lies in the Jeddah terrane of the West-central Arabian Shield. It is about 50 km east of Mahd Adh Dhahab city and 300 km northeast of Jeddah. It has an elliptical overall planform (~8.5 km by 11.5 km) and lies between latitudes 23°30’ and 23°37’ N and longitudes 41°70’ and 41°15’ E (Fig. 2). U–Pb zircon dating of the intrusion yielded ages of 625-613 Ma (Ali et al., 2014).

The Ad-Dayheen intrusion is composed of a series of discontinuous alkaline/peralkaline granitoid ring dikes and diapirs. The ring dikes were later displaced across left-lateral strike–slip structures. Most of the core area and all the margins of the Ad-Dayheen intrusion are covered by Quaternary Wadi deposits. The Ad-Dayheen granitoids show marked variation in color, texture

and composition. They include monzogranite, syenogranite, alkali feldspar granite, alkaline/peralkaline granite, microgranite and pegmatite.

Monzogranite is the earliest unit of the Ad-Dayheen intrusion. It outcrops as a few small (<1 km), low-relief knobs in the low-lying land at the core of the complex. It is coarse- to medium-grained and occasionally porphyritic with light gray to pale pink or grayish-pink color. The contacts between the monzogranite and the other rock types of the complex are not exposed. A few small dikes of andesite and basalt are observed within the monzogranite knobs; none are long enough to extend to the rim of an individual knob.

The syenogranite and alkali feldspar granite were previously grouped and described as amphibole-biotite granites (Moghazi et al., 2011), because they are difficult to distinguish in the field. They form the bulk of the Ad-Dayheen intrusion and occur as ring dikes and arcuate plutons surrounding the monzogranite. The contacts between syenogranite and alkali feldspar granite are gradational, obscure in outcrop, and defined only by changes in modal plagioclase content. The syenogranite and alkali feldspar granite are devoid of xenoliths, rarely intruded by dikes, and have variable colors from gray to reddish-brown and variable grain sizes from medium-grained to porphyritic.

The alkaline and peralkaline granites occur as incomplete ring dikes and masses emplaced into the inner ring of alkali feldspar granite plutons with sharp, steeply-dipping intrusive contacts. They stand as high, irregular, crescent-shaped outcrops. The alkaline/peralkaline granites are medium-grained to slightly porphyritic and pinkish-grey. Highly mineralized peralkaline granitic dikes, aplite dikes, and quartz veins crosscut the host alkaline granite. Locally, the quartz veins display ductile deformation. The intrusive relations clearly indicate that the alkaline and peralkaline granites are younger than the monzogranite,

syenogranite and alkali feldspar granite. A few roof pendants of alkali feldspar granite occur above the peralkaline granite (Fig. 3a) and angular and flattened xenoliths (10 to 40 cm) of alkali feldspar granite are common in the peralkaline granite.

Locally, isolated bodies of porphyritic microgranite with complex contacts are observed within the syenogranite and alkali feldspar granite (Fig. 3b). Microgranite is a subvolcanic phase with the same mineralogical composition as alkali feldspar granite but a much finer-grained texture. The microgranite is likely the chilled carapace of the typical alkali feldspar granite.

Pegmatitic pockets and dikes, fluorite veins, quartz veinlets and miarolitic cavities are common in the peralkaline granite. Pegmatite occurs as sheet-like bodies (Fig. 3c), pockets along the edges of the peralkaline granite, or within fault zones. Pegmatites at the outer margins of alkaline/peralkaline granite show gradational boundaries. Fluorite and quartz veins occur between alkali feldspar granite and pegmatite.

3. Analytical methods

Mineral identification was accomplished using polarizing petrographic microscopy, environmental scanning electron microscopy (ESEM), electron probe micro-analysis (EPMA), powder X-ray diffraction (XRD), and micro-Raman spectroscopy. The Philips XL30 ESEM at the Nuclear Materials Authority in Egypt is equipped with an EDAX energy dispersive X-ray spectrometer able to detect elements as light as boron; it was operated at 25 kV and counting rates were kept between 1000 and 1500 per second. The BRUKER D8 advanced XRD in the Central Metallurgical and Development Institute, Cairo, Egypt, used Cu radiation with a secondary monochrometer and was operated at 40 kV and 40 mA, with a scan speed 1 °/min in 2θ. Mineral identification referenced *d*-spacing and relative intensities of reflections in the American Standard Test Materials (ASTM) cards.

EPMA analyses of polished, carbon-coated sections were carried out in two laboratories. The Division of Geological and Planetary Sciences, California Institute of Technology, USA, has a five-spectrometer JEOL JXA-8200. It was operated at 15 kV with a 25 nA focused (~1 μm) beam, 20 s on-peak counting times, mean-atomic number background subtraction method, a mix of natural and synthetic mineral standards, and the CITZAF matrix correction routine. Selected mineral identifications were spot-checked with a Renishaw InVia micro-Raman spectrometer using a 514 nm Ar-ion laser and comparison to the RRUFF mineral spectra library. The Department of Geosciences, University of Oslo, Norway, has a CAMECA SX100 electron probe. It was operated at 15 kV with a 15 nA, 2 μm diameter beam for 10 seconds counting time on-peak and 5 seconds each at low and high background positions. A ZAF matrix correction routine was used.

Based on the petrographic studies, 34 rock samples were selected for major, trace and rare-earth element analyses at Activation Laboratories Ltd. (Actlabs), Canada. Samples were crushed in an agate mortar, quartered several times to obtain representative splits, and powdered to ~40 mesh in an agate ring mill. The major oxides were measured by lithium metaborate/tetraborate fusion ICP-AES. Trace and rare earth elements were measured by ICP-MS following lithium borate fusion and acid digestion. Loss on ignition (LOI) was determined by weight difference after firing at 1000 ºC. Precision and accuracy were controlled by analysis of international reference materials and replicate analyses and are 1% for major elements and 2% to 5% for trace elements. Details of analytical precision, standardization, and detection limits are given on the Actlabs website (actlabs.com).

4. Petrography

Petrographic examination supports the division of the Ad-Dayheen intrusion into monzogranite, syenogranite, alkali feldspar granite, alkaline/peralkaline granites, microgranite, pegmatite, and quartz veins. The petrographic description of each rock type is given below.

4.1. Monzogranite

Monzogranite is inequigranular, medium- to coarse-grained, and pink. It consists essentially of K-feldspar (30–45 vol.%), quartz (25–35 %), plagioclase (15–25 %), and mafic minerals (<5 %), with accessory Fe-Ti oxides, fluorite, titanite, zircon, apatite and allanite. K-feldspars occur as large anhedral crystals of perthite with string textures and small plagioclase inclusions. Anhedral to subhedral quartz occupies interstices between the feldspars or forms graphic and myrmekitic intergrowths with K-feldspar. Plagioclase occurs as euhedral to subhedral tabular crystals, usually zoned and corroded, and with selectively sericitized cores. The mafic minerals include mainly biotite and rare hornblende. Biotite forms subhedral crystals or anhedral flakes; it is strongly pleochroic from straw yellow to deep brown **(Fig. 4a).** Biotite is associated with titanite, contains small inclusions of zircon, and is partially altered to chlorite. Hornblende is rare and occurs as fine-grained prismatic crystals. Zircon occurs as small prismatic crystals that show oscillatory zoning.

4.2. Syenogranite and alkali feldspar granite

The syenogranite and alkali feldspar granite are medium- to coarse-grained with porphyritic texture. They essentially consist of alkali feldspars (40-60 %) and quartz (20-30 %), with variable amounts of plagioclase (2-15 %), mafic minerals (1-3 %), and accessory zircon, allanite, fluorite, apatite, pyrochlore, samarskite and xenotime. The modal abundance of plagioclase and mafic minerals decrease from syenogranite to alkali feldspar granite. K-feldspar occurs as phenocrysts and as fine- to medium-grained anhedral crystals of perthite and minor

microcline. Perthite shows a variety of textures (vein, flame and patchy) and contains small inclusions of albite, biotite and zircon. Graphic textures of quartz and K-feldspars are common, especially in the alkali-feldspar granite. Albite is the only plagioclase in the alkali feldspar granite and contains many inclusions of apatite (Fig. 4b). In the porphyritic samples, the albite crystals show flow-alignment. Quartz is not uniform in distribution or amount. It occurs as large porphyritic crystals containing abundant inclusions of albite or as fine-grained anhedral crystals. Some large quartz crystals in the alkali feldspar granite show snowball texture, defined by laths of albite arranged concentrically along growth zones (Fig. 4c). The snowball quartz crystals are subhedral to euhedral, uniform in size and may contain a few inclusions of biotite. The mafic minerals include biotite with minor amphiboles. Biotite occurs as long crystals or fine flakes, reddish-brown in color and moderately pleochroic. The amphibole occurs as subhedral to anhedral elongated crystals or tends to form aggregates with the Fe-Ti oxides. It is strongly pleochroic and petrographically defined as hornblende. Some crystals exhibit spongy or sieve-like texture due to abundant inclusions. Zircon occurs as small prismatic crystals that rarely show oscillatory zoning.

4.3 Alkaline and peralkaline granites

The alkaline and peralkaline granites are medium- to coarse-grained, with hypidiomorphic to porphyritic textures. Samples are homogeneous in modal composition, except for some variation in the abundance of alkali amphiboles. They consist of K-feldspars (20-30 %), albite (25-30 %), quartz (35-40 %), mafic minerals (5-15 %), and accessory zircon, allanite, muscovite, fluorite, apatite, rutile, Fe-Ti oxides, xenotime, samarskite and pyrochlore. K-feldspar forms subhedral to anhedral, tabular to equant crystals of orthoclase- and microcline-microperthite with a few inclusions of plagioclase and zircon. In places, large K-feldspar crystals

are rimmed by albite. Albite occurs as fine-grained laths that occasionally show parallel arrangement. Quartz occurs as resorbed phenocrysts or forms anhedral interstitial crystals intergrown with K-feldspars in a graphic texture. Some large quartz crystals contain tiny inclusions of the mafic minerals and feldspars. Plagioclase crystals are very rare, occurring only as inclusions in perthite. The mafic minerals include aegirine and sodic amphibole. Aegirine occurs as fine or medium, subhedral to euhedral prismatic or acicular crystals (Fig. 4d). A few aegirine crystals contain inclusions of monazite (Fig. 4e). The sodic amphibole is petrographically identified mainly as arfvedsonite and contains inclusions of K-feldspars, zircon and apatite (Fig. 4f).

Apatite occurs as fine needles, while Fe-Ti oxides occur either as individual crystals or as granular aggregates associated with altered mafic minerals. Zircon occurs as interstitial crystals showing oscillatory zoning or as inclusions within feldspars and arfvedsonite (Fig. 4f). Some secondary zircons associated with monazite appear to have formed at the expense of amphibole (Fig. 4g). Fluorite occurs as anhedral interstitial crystals among the feldspars and rarely as veins filling fractures. Allanite is common as strongly pleochroic reddish-brown anhedral crystals (Fig. 4h). Muscovite occurs as subhedral to euhedral medium-grained crystals among other rock-forming minerals. Pyrochlore forms yellow to reddish-yellow subhedral crystals, mostly as inclusions in aegirine. Monazite occurs as separated crystals, in aggregates with zircon, and as inclusions in aegirine.

4.4. Microgranite

Microgranite displays a typical fine-grained subvolcanic texture; it is mostly allotriomorphic, but porphyritic and granophyric textures are also widespread. Phenocrysts of K-feldspars, albite, quartz and mafic minerals are embedded in a fine matrix of mostly quartz and

K-feldspar. Accessory minerals include Fe-Ti oxides, zircon, pyrochlore, apatite, titanite, fluorite, monazite and xenotime. Rectangular crystals K-feldspars show perthitic texture. The plagioclase phenocrysts are tabular crystals of albite, usually fresh and twinned. Quartz occurs as mostly corroded anhedral phenocrysts or micrographic intergrowths with K-feldspar in the groundmass. The mafic minerals (<5 % in total) are aegirine, sodic amphiboles and biotite. The sodic amphiboles include both riebeckite and arfvedsonite (Fig. 4i, j), as subhedral to euhedral individual crystals or as fine clusters. Aegirine is observed in a few samples as anhedral spongy crystals or as acicular crystals. Small biotite flakes are enclosed in the graphic groundmass. In the mineralized microgranite samples, zircon is present as aggregates of reddish-brown subhedral to anhedral crystals, associated with monazite. Some zircon crystals show patchy zoning and have a spongy texture with abundant fluid and mineral inclusions. Pyrochlore occurs as primary yellow to reddish-yellow subhedral crystals or as a secondary mineral replacing primary fergusonite. Monazite occurs as subhedral isolated crystals or as anhedral cracked inclusions within the aegirine. Xenotime occurs as interstitial grains between K-feldspars (Fig. 4k) or as overgrowths on euhedral zircon. Fergusonite occurs as small anhedral zoned crystals mostly replaced by pyrochlore.

4.5. Pegmatite

The pegmatite is very coarse-grained and pink to pinkish-white. It consists essentially of quartz, K-feldspars, and minor mafic minerals. Accessory minerals vary in identity and proportion among samples and include zircon, pyrochlore, bastnaesite, fergusonite, xenotime, thorite, beryl, fluorite, synchysite, doverite, senaite, columbite-tantalite, samarskite and aeschynite. K-feldspars are coarse-grained, subhedral to anhedral prismatic crystals of orthoclase and microcline. Microcline shows tartan twinning and is usually intergrown with albite, forming

patchy perthite. The mafic minerals include mostly sodic amphibole (arfvedsonite and riebeckite, Fig. 4l, m) with lesser aegirine and biotite. Aegirine occurs as acicular crystals partly altered to hematite. Zircon is the most common accessory mineral and occurs as isolated reddish-brown subhedral prismatic crystals or as inclusions in the sodic amphibole (Fig. 4m). Zircon also occurs as anhedral clusters of spongy crystals with abundant fluid inclusions; texturally the zircon clusters appear to replace aegirine and are associated with hematite and bastnaesite. Fergusonite is the main Nb mineral and occurs as dark brown prismatic crystals (Fig. 4n), sometimes optically zoned, and altered to pyrochlore at the rim. Pyrochlore replaces fergusonite or forms rounded yellowish-brown grains.

4.6. Quartz veins

Quartz veins consist essentially of quartz with minor amounts of perthite and aegirine. The accessory minerals include cassiterite, pyrochlore, zircon, fergusonite, gadolinite, britholite, bastnaesite and sphalerite. Quartz shows variable degrees of ductile deformation. Aegirine occurs as fine needle-shaped crystals. Pyrochlore occurs as patchily zoned anhedral crystals associated with aegirine. Zircon occurs as anhedral equant or prismatic crystals with abundant fluid and mineral inclusions. Fergusonite is the main Nb mineral in the quartz veins.

5. Mineral chemistry

The identification of the minerals under the microscope was refined and supported by EPMA analyses. The essential silicate minerals were analyzed in samples of syenogranite, alkali feldspar granite, alkaline granite, and peralkaline granite (Supplementary Tables 1S-11S).

5.1. Pyroxene

Pyroxene analyses in alkali feldspar granite, alkaline granite and peralkaline granite are reported in Supplementary Table 1S. They are sodic pyroxene with high Na_2O (9.0-14.1 wt.%)

and FeO* (23.5-31.2 wt.%) contents and low but variable concentrations of Al_2O_3 (0.1-0.6 wt.%), TiO_2 (0.6-4.0 wt.%), CaO (0.1-8.4 wt. %), MgO (0.1-4.0 wt.%), and K_2O (<0.02 wt.%). In the classification scheme of Morimoto et al. (1988), the pyroxene analyses extend from aegirine to aegirine-augite (Fig. 5a).

5.2. Biotite

Biotite was only analyzed in syenogranite (Supplementary Table 2S). Biotite analyses are mostly iron-rich and classify as annite. Despite some variability, all biotite analyses plot in the primary field in the $10*TiO_2$-(FeO+MnO)-MgO diagram (Fig. 5b) of Nachit et al. (2005). The composition of biotites reflects the composition and oxidation state of the parent magma (Nachit et al., 1985; Abdel-Rahman, 1994; Bucholz et al., 2018); the average Fe/(Fe+Mg) = 0.58±0.02 is rather high and implies the presence of plenty of Fe^{2+} in the system at the time of biotite crystallization. On the Al_2O_3 vs. $FeO^{(t)}$ discrimination diagram of Abdel-Rahman (1994), the biotite analyses plot in the alkaline field (Fig. 5c).

5.3. Amphibole

The compositions of amphiboles from the syenogranite, alkali feldspar granite and peralkaline granite are reported in Supplementary Table 3S. All the analyzed amphiboles contain >0.1 Ti a.p.f.u., a characteristic of primary igneous amphiboles (Girardeau and Mevel, 1982). The amphiboles of the alkali feldspar granite and peralkaline granite are rich in sodium. Following the classification of Hawthorne et al. (2012), as implemented in the spreadsheet by Locock (2014), the amphiboles in syenogranite are ferro-edenite to ferro-actinolite, those in the alkali feldspar granite are uniformly ferri-katophorite, and those in the peralkaline granite are mostly arfvedsonite with some potassic-arfvedsonite and some riebeckite. In the Na_2O vs. FeO^T

diagram of Pe-Piper (2007), the sodic amphiboles mainly plot in the field of primary magmatic amphiboles (Fig. 5e).

5.4. Aenigmatite

Aenigmatite is a pyroxenoid, ideally $Na_2Fe^{2+}_5TiSi_6O_{20}$. Aenigmatite is only recorded in peralkaline granite and is close to the nominal composition (Supplementary Table 4S), except for minor substitution of MnO (2.1-2.2 wt.%) for FeO.

5.5. Feldspars

Plagioclase, albite, and K-feldspar analyses are reported in Supplementary Tables 5S, 6S and 7S. Plagioclase was only analyzed in syenogranite and is represented by oligoclase (An_{12-14}). K-feldspar is much more abundant than albite in all the granitic rocks of the Ad-Dayheen intrusion. Albite is, however, present in all the rock types and is nearly uniform end-member $NaAlSi_3O_8$, with very low CaO content (<0.1 wt.%). K-feldspars are near end-member $KAlSi_3O_8$, also with CaO < 0.1 wt.%.

5.6. Fe-Ti oxides

Fe-Ti oxides are the most common opaque accessory phases in the Ad-Dayheen granites, mainly magnetite, ilmenite and goethite. Representative analyses of magnetite from syenogranite, alkali feldspar granite and alkaline granite are presented in Supplementary Table 8S. In alkali feldspar granite and alkaline granite, magnetite is near end-member Fe_3O_4 ($TiO_2 \leq$ 1.9 wt.%, MnO $\leq$ 0.70 wt.%), whereas in syenogranite magnetite contains variable TiO_2 extending to rather high concentrations (1.4-9.9 wt.%). Ilmenite was analyzed in alkali feldspar granite and alkaline granite (Supplementary Table 9S). Most ilmenite occurs in association with magnetite. The analyzed ilmenite is rich in MnO (3.4-10.9 wt.%). Representative analyses of goethite are presented in Supplementary Table 10S. It has low analytical totals (<88 wt.%) and

the main oxide is FeO^T with considerable and variable amounts of SiO_2 (4.1-22.0 wt.%). These analytical spots are presumably very fine-grained aggregates whose mineralogy is not resolvable in detail at electron probe scale; Raman spectra obtained with a ~1 μm laser spot confirm the presence of goethite as the main phase but do not exclude admixture of other minerals.

5.7. Titanite

Titanite is only analyzed in the alkali feldspar granite (Supplementary Table 11S). It shows limited compositional variation. The main oxides are SiO_2 (29.5-30.0 wt.%), TiO_2 (36.9-37.8 wt.%) and CaO (24.9-25.5 wt.%), with minor amounts of FeO^T (1.0-1.6 wt.%).

6. Whole rock geochemistry

6.1. Geochemical characteristics

Whole-rock geochemical data (major, trace and rare-earth elements) and calculated normative mineral compositions of 34 samples representing the petrological varieties of the Ad-Dayheen intrusion are given in Tables 1, 2 and 3. The granitoid rocks extend from 70.6-76.8 wt.% SiO_2; the highest SiO_2 concentrations are in the pegmatite samples. On the R_1-R_2 diagram of De la Roche et al. (1980), most analyses plot in the alkali granite field (Fig. 6), but monzogranite plots on the boundary between the granite and alkali granite fields and the low-silica samples of microgranite and peralkaline granite extend into the quartz syenite field. These classifications are consistent with the petrographic nomenclature of the samples.

Major element compositions are shown in SiO_2 variation diagrams in Fig. 7. The contents of TiO_2, Al_2O_3, MgO, CaO, and (to a lesser extent) K_2O decrease with increasing SiO_2 (Fig. 7a, b, d, e and f), whereas Fe_2O_3 increases slightly and Na_2O does not show a distinct trend (Fig. 7c and g). Total alkali content (Na_2O+K_2O) is nearly independent of SiO_2 (Fig. 7h). In most of these variation diagrams, the entire dataset scatters broadly about a single trend, but dividing the

samples by petrographic type reveals important deviations from a single trend, especially in Na_2O vs. SiO_2 (Fig 7g), where each petrographic type (except microgranite) forms a distinct subparallel trend.

Trace element concentrations vary widely among granitoids (excluding pegmatites) from the suite but show significant clustering by petrographic type (Fig. 8). Some trace elements show an overall correlation with SiO_2 in the entire sample suite (e.g., Ga), while others appear scattered (e.g., Rb); however, variation diagrams for most trace elements against SiO_2 again reveal subparallel trends for each petrographic type, akin to those noted for Na_2O. Similar ranges of variability in trace element enrichment have been described in other alkaline granites in Saudi Arabia (Moghazi et al., 2011; Moufti et al. 2013; Abdalla et al., 2020; Abuamarah, 2020). The monzogranite and syenogranite are systematically richer in Ba (305-541 μg/g) and Sr (154-274 μg/g) than the alkali feldspar granites (202-289 μg/g Ba, 123-158 μg/g Sr) and alkaline/peralkaline granites (74-202 μg/g Ba, 23-93 μg/g Sr). On the other hand, the alkaline/peralkaline granites are richer in Nb (66-132 μg/g), Y (112-199 μg/g), Zr (807-1352 μg/g), Ta (6-13 μg/g), Hf (21-45 μg/g), and Th (18-27 μg/g) than the other rock types. The subvolcanic microgranite shows evidence of substantial enrichment in Nb, Zr, Ta, Th, and U compared to the plutonic-textured samples of peralkaline granite. Trace element concentrations exhibit extreme enrichments in the pegmatite samples (Table 1), with very high abundances of Nb (1351-2047 μg/g), Y (828-2238 μg/g), Ta (95-156 μg/g), Hf (131-377 μg/g), Th (244-600 μg/g), U (81-179 μg/g), Zr (2397-14927 μg/g), Sn (94-127 μg/g) and Cs (17-77 μg/g). For purposes of tectonic discrimination and classification of the intrusion, we will set aside the highly mineralized microgranite and pegmatite samples.

Primitive-mantle-normalized multi-element diagrams for the averages of each petrographic rock type are shown in Figure 9a. The microgranite and pegmatite samples are highly enriched in many elements. It is clear that the different rock types show general similarities in their patterns. They are enriched in some large-ion lithophile elements (LILE: Rb, K, Th) and high field strength elements (HFSE: Ta, Nb, Zr, Hf), but strongly depleted in Ba, Sr, P and Ti, consistent with an A-type granite geochemical signature (Wu et al., 2002).

REE concentrations and diagnostic parameters based on ratios of REEs are listed in Table 3 and the chondrite-normalized REE patterns are presented in Figure 9b. The suite displays essentially parallel REE patterns that span a wide range in total REE contents, well correlated with petrologic type. ∑REE increases from monzogranite (83-200 μg/g) through syenogranite (190-206 μg/g), alkali feldspar granite (224-271 μg/g), alkaline granite (287-386 μg/g), peralkaline granite (332-701 μg/g), microgranite (899-1641 μg/g), and pegmatite (1969-4761 μg/g). All patterns are enriched in light rare-earth elements relative to heavy rare-earth elements, indicated by $(La/Lu)_n$ = 1.81-9.38, with patterns generally becoming flatter overall as they grow more enriched.

All samples have negative Eu anomalies. The monzogranite, with the lowest ∑REE content, has Eu/Eu* = 0.30-0.35 and $(La/Lu)_n$ = 6.22-9.38. The syenogranite and alkali feldspar granite have slightly more negative Eu anomalies (Eu/Eu*= 0.23-0.32) and flattening patterns, with $(La/Lu)_n$ = 4.12-5.57 in the syenogranite and 4.83-6.13 in the alkali feldspar granite. The alkaline and peralkaline granites show very similar REE patterns with still deeper Eu anomalies (Eu/Eu*=0.17-0.25). The increasingly negative Eu anomalies and strongly decreasing concentrations of Ba and Sr suggest continuing fractionation of feldspars (Lee et al., 2013), but

may also be explained by fractionation of fluorite or by open-system processes involving F-rich fluids.

The trend of increasing concentration of REEs, increasingly negative Eu anomalies, and flattening overall REE slope continues through the microgranite (Eu/Eu* = 0.11-0.16, $(La/Lu)_n$ = 4.34-6.31) and into the highly enriched pegmatites, with ∑REE = 1969-4761 μg/g, Eu/Eu* = 0.13-0.15, slightly fractionated LREE ($(La/Sm)_n$=1.94-2.24), and nearly flat HREE ($(Gd/Lu)_n$= 0.97-1.15).

6.2. Magma type

The studied rocks have high $FeO^T/(FeO^T+MgO)$, high alkali contents, marked enrichment in REE, Zr, Nb, Th, Hf, Ta and Y, and depletion in Sr, Ba, P, Eu, Co, Sc and V. All these features are diagnostic of the A-type affinity of the Ad-Dayheen intrusion (Küster, 2009). Excepting the monzogranite and some syenogranite samples, the rest of the suite contains sodic amphibole and sodic pyroxene in the mode and acmite and Na-metasilicate in the norm (Table 2), all distinctive features of alkaline and peralkaline rocks.

The $Al_2O_3/(CaO+Na_2O+K_2O)$ (A/CNK) values of the analyzed samples decrease through the petrological types, confirming the increasingly alkaline character of the suite from monzogranite to peralkaline granite. A/CNK values are 0.86-0.97 in monzogranite, 0.89-0.91 in syenogranite, 0.80-0.91 in alkali feldspar granite, 0.77-0.81 in alkaline granite, 0.77-0.81 in peralkaline granite, 0.79-0.92 in microgranite, and 0.67-0.88 in pegmatite (Table 1). The high agpaitic index [AI = (Na+K)/Al (atom %)] of the studied rocks (0.91-0.96 in monzogranite, 1.0-1.01 in syenogranite, 1.01-1.12 in alkali feldspar granite, 1.15-1.20 in alkaline granite, 1.14-1.21 in peralkaline granite 1.03-1.23 in microgranite and 1.19-1.37 in pegmatite) again confirm their increasingly alkaline and peralkaline nature (Liégeois and Black, 1987; Liégeois et al., 1998).

The alkaline affinity of the investigated granites can be confirmed with the granite classification diagram of Sylvester (1989) (Fig. 10a). Notably, on this diagram the sequence of petrologic types trends away from the "highly fractionated granite" field, deeper into the alkaline field, with increasing SiO_2. On the FeO^T/MgO vs. Ga/Al discrimination diagram of Whalen et al. (1987), all analyzed Ad-Dayheen samples plot in the A-type granite field (Fig. 10b). According to the discrimination diagrams of Eby (1992), the granite samples plot mainly in the A_2-type field (Fig. 10c, d), except that the (extensively mineralized) microgranite and pegmatite samples plot in the A_1-type field. A_1-type granites are thought to represent anorogenic mantle-derived magma, whereas A_2-type granitoids form in post-orogenic settings from subcontinental lithosphere or lower crustal sources (Eby, 1992).

7. Discussion

One of the most striking features of the northernmost segment of the ANS is the abundance of post-collisional felsic plutons, including both calc-alkaline and alkaline/peralkaline granitoids (Eyal et al., 2010; Abuamarah, 2020; Abuamarah et al., 2020; Abdallah et al., 2020). The evolution of the Ad-Dayheen intrusion is discussed here in light of the current data and the larger context of post-collisional magmatism in the northern ANS.

7.1. Geodynamic setting

Our results from field relationships, petrography, mineralogy, mineral chemistry, and bulk chemistry all help to define the tectonic evolution and geodynamic significance of the Ad-Dayheen intrusion. First and foremost, intrusive contact relations show that the Ad-Dayheen intrusion is post-collisional, being younger than the surrounding subduction-related rocks. In the study area, swarms of early post-collisional calc-alkaline dikes ranging in composition from rhyolite to basalt cut the subduction-related calc-alkaline rocks and are, in turn, truncated by the

Ad-Dayheen ring complex. Moreover, the chemical characteristics of the Ad-Dayheen intrusion are consistent with a within-plate tectonic setting: they have alkaline/peralkaline character; marked depletion in CaO, MgO, Sr, and transition metals; high alkali contents; and primitive-mantle-normalized trace element patterns (Fig. 9a) enriched in both LILE and HFSE with no anomalies in Nb or Ta (Pearce et al., 1984).

The Rb vs. Nb+Y tectonic discrimination diagram of Pearce et al. (1984) indicates a within-plate geochemical affinity (Fig. 11a); only monzogranites straddle the boundary with volcanic arc granites. On the multicationic diagram of Batchelor and Bowden (1985), the studied samples straddle the post-orogenic to anorogenic granite fields (Fig. 11b); again, only the monzogranite straddles the boundary with syn-collisional rocks.

The compositions of biotite, amphibole and pyroxene in the Dayheen granites confirm the inferences from whole-rock geochemistry that the studied samples are alkaline to peralkaline rocks with anorogenic affinities (Nachit et al., 1985; Abdel-Rahman, 1994). On the biotite discrimination diagram (Figs. 5c, d), all biotite data from syenogranite plot completely in the alkaline anorogenic and alkaline/peralkaline fields. Pyroxenes were identified as sodic pyroxenes (aegirine) (Fig. 5a) and amphiboles include sodic varieties such as arfvedsonite and riebeckite; these are commonly the mafic constituents of highly alkaline rocks (Samuel et al., 2007; Azer et al., 2014).

7.2. Magma sources

A complete spectrum of petrogenetic models from entirely mantle-dominated to entirely crust-dominated have been proposed for A-type alkaline magmatism in the ANS, but no single model has been suggested that satisfactorily explains all their chemical features. Geochemical modeling has led some authors to invoke fractional crystallization of mantle-derived mafic

magmas (e.g., Muskhin et al., 2003; Jarrar et al., 2008), while others have considered that the same rocks represent anatectic melts of various crustal sources (Moghazi et al., 2011; Moufti et al., 2013). Indeed, the large range in major and trace element concentrations and in isotope ratios among the various A-type granitoids and associated volcanic units in the ANS seem to demand that a variety of processes and sources were involved. Compromise models have invoked mantle origins with significant crustal contributions (e.g., Be'eri-Shlevin et al., 2009; Abdallah et al., 2020). Recent studies attribute this persistent controversy to the small contrast in radiogenic isotope ratios of young juvenile crust and upper mantle (Hargreave et al., 2006; Eyal et al., 2010); at the time of post-collisional magmatic activity, there had not been enough time for ingrowth of a distinctive radiogenic signature in the ANS crust (Eyal et al., 2010; Morag et al., 2011).

The pioneering work on the genesis of the Ad-Dayheen intrusion by Moghazi et al. (2011) concluded that all the granitic rocks of the intrusion were cogenetic, with a primary magma that originated by partial melting of juvenile lower crust. However, our field work demonstrates that the Ad-Dayheen complex consists of a series of intrusive events and we will test whether the various magmatic phases were derived from different sources.

Eby (1992) has shown that fractionation of A-type magmas has very little or negligible effect on the Y/Nb ratio and that an Y/Nb ratio of 1.2 forms the boundary between magmas derived from mantle sources (A_1-type, Y/Nb < 1.2) and crustal sources (A_2-type; Y/Nb > 1.2). Although the heavily mineralized microgranite and pegmatite have Y/Nb < 1.2, all other samples of the intrusion have Y/Nb > 1.2, indicating crustal sources. On the discrimination diagrams of Eby (1992), all Ad-Dayheen samples except microgranite and pegmatite lie in the A_2-type fields **(Fig. 10c, d)**. We suggest that these results can be interpreted to reflect dominantly crustal sources for the primary magmas of the Ad-Dayheen intrusion, modified in the microgranite and

pegmatite by a late mineralization process that specifically enriched these rocks in Nb. The dominant role of continental crust in the evolution of the Ad-Dayheen intrusion is supported by high concentrations of incompatible elements and low Sr contents in the more felsic members. K/Rb and Rb/Zr ratios do not significantly change during fractional crystallization of magma (before the appearance of K-feldspar and zircon on the liquidus) but are changed by contamination (Davidson et al., 1988). Both K/Rb (95-353) and Rb/Zr (0.02-0.98) systematically decrease with increasingly evolved petrologic type across the whole Ad-Dayheen suite, not just in the heavily mineralized members (Table 1). Hence, even if the most primitive members of the suite (monzogranites) are derived from deep crustal sources, simple fractional crystallization will not generate the more evolved members of the suite. Contamination by an additional component is required. That is, a primary magma derived from melting of one crustal source must have reacted, either with higher-level crustal materials or with a mantle-derived component, before or during its evolution towards the highly evolved members. This conclusion is confirmed by quantitative fractionation modeling, detailed below. The absence of mafic lithologies, enclaves, xenoliths, or xenocrysts in the Ad-Dayheen intrusion argues against an origin from fractional crystallization of mantle-derived mafic magma (Azer, 2013).

The relatively flat HREE patterns observed in the Dayheen granites imply a garnet-free source and therefore relatively shallow depths of magma genesis (Azer et al., 2014), which is not surprising given the rather low estimated crustal thickness for the ANS at the time of their genesis. Oxygen isotope data for various A-type rocks in the north ANS strongly support arguments against a pure mantle origin of silicic magma and favor a major contribution of upper crust (Be'eri-Shlevin et al., 2009). Oxygen isotope ratios in bulk zircon separated from Ad-Dayheen granites in particular range from $\delta^{18}O$ = +3.2 to +6.4 ‰ (Ali et al., 2014), whereas

zircons from mantle-derived magmas preserve homogeneous initial magmatic values of $\delta^{18}O$ = 5.3±0.6 ‰ (Valley et al., 1998). The Ad-Dayheen granites have positive $\varepsilon_{Hf}(t)$ values (+5 to +8.8); although positive ε_{Hf} conventionally indicates depleted mantle sources, it is equally consistent with derivation from young juvenile crust (Ali et al., 2014). "Mantle" radiogenic signatures in A-type rocks throughout the ANS can be attributed to the young age of Pan-African crust during the post-collisional stage, though this does not exclude metasomatism by mantle-derived fluids or influence of mantle heat sources (Morag et al., 2011).

7.3. Magmatic evolution

Field relations and chemical data indicate that the Ad-Dayheen ring complex was emplaced in a series of magmatic pulses, each beginning at a similar SiO_2 content but extending to more evolved and geochemically enriched compositions than the one before. The isolated monzogranite at the center of the complex is probably the first pulse. We infer that the next phase is the surrounding ring of syenogranite and alkali feldspar granite, which was then intruded by alkaline and peralkaline granite, topped by subvolcanic microgranite and finally cut by dikes of pegmatite. While the general compositional trends of most major oxides (Fig. 7), trace elements (Fig. 8) and rare earth elements (Fig. 9b) are broadly consistent with expectations for simple progressive fractional crystallization of a cogenetic suite, there are significant anomalies that require further investigation. As noted above, when major element variation diagrams are plotted with different symbols for each petrologic type, a series of subparallel trends emerge, especially in Na_2O vs. SiO_2. The same is true of many trace elements (Fig. 8) and, as pointed out above, the Rb vs. K/Rb (Fig. 12a) and Rb/Zr ratios (Table 1) appear to indicate that progressive contamination (or perhaps post-magmatic modification) is required in addition to fractional crystallization. The MORB-normalized spider diagram for the averages of each

granite type (Fig. 9a) indicate steadily growing negative anomalies in Sr, Ba, P and Ti alongside increasingly negative Eu anomalies and nearly constant K contents (Fig. 9b). The Sr, Ba, and Eu anomalies seem consistent with plagioclase fractionation, yet plagioclase is scarce in the observed rocks. Constant K_2O despite progressively increasing K/Rb (Fig. 12a) with increasing SiO_2 indicates some role for alkali feldspar removal. Correlations of Eu anomalies with Sr, CaO and Nb (Fig. 12b, c, d) suggest a common process influencing all these elements, except perhaps in microgranite and pegmatite. P and Ti anomalies most likely reflect fractionation of apatite and Fe-Ti oxides, respectively.

The investigated granites have a hypersolvus nature that indicates low water pressure and high temperatures of crystallization, similar to other alkaline rocks emplaced at relatively shallow depth (King et al., 1997). Furthermore fluorine has significant effects on the physico-chemical properties of granitic magma. The presence of magmatic fluorite at Ad-Dayheen resembles that in other F-rich granites, such as the Aja complex in Saudi Arabia (Abuamarah, 2020; Abdallah et al., 2020). The solubility of water in melts decreases in the presence of fluorine (Dingwell, 1985), but fluorine lowers the crystallization temperature as effectively as water, implying not only low water pressure but low total pressure and volatile content, in order to stay above the alkali feldspar solvus. Fluorine also effectively lowers the viscosity of granitic magmas, which may have promoted faster migration of melt and allowed emplacement at shallow levels (Hannah and Stein, 1990). The source of F-rich fluids in granitic systems has been attributed variously to magmatic (e.g., Cuney et al., 1992) and metasomatic sources (e.g., Nurmi and Haapala, 1986); in the Ad-Dayheen case magmatic fluorite is present already in the most primitive members (monzogranite and syenogranite) of the suite and so F was not a late hydrothermal addition to the system.

A ternary projection of normative Qz–Ab–Or contents (Fig. 13a) shows that the Ad-Dayheen suite plots along the trace of vapor-saturated minimum melt compositions at low pressure with 1 to 4 wt.% F in the fluid phase (Manning, 1981). The monzogranite samples plot close to the fluorine-free minimum, whereas the rest of the suite trends toward higher F concentrations. Although F concentration in the fluid might increase during simple fractional crystallization, this depends on the relative bulk partition coefficients of H_2O and F (London et al., 1988; Manning, 1981). It is also possible that F-bearing components were assimilated during magma evolution. A quantitative model is required to distinguish these cases. The accumulation of volatiles and trace elements ultimately led to the development of pegmatites and veins at the end of the magmatic phase.

We tested the role of fractional crystallization and other open-system processes in generating the compositional variations in the Ad-Dayheen intrusion using the rhyoliteMELTS model of Gualda et al. (2012), as implemented in the alphaMELTS 1.9 code (Smith and Asimow, 2005), which tracks both major and trace elements during magmatic processes. We used the default set of pressure, temperature, and composition dependent mineral/melt partition coefficients. We note in advance that this model can only offer an incomplete description of the Ad-Dayheen system because it does not explicitly include fluorine or a number of the accessory phases that appear, especially in the more evolved members of the suite. However, as we have noted, the differences among the compositional evolution of the three magmatic pulses are manifest already in the least evolved members of each group, where F concentrations are lowest and accessory phases have not yet saturated. Furthermore, our fundamental conclusion that a process other than fractional crystallization is required to explain all the data is evident from the data, even before application of a model.

To test whether the entire Ad-Dayheen suite might represent a simple fractional crystallization trend, we selected the most primitive monzogranite (Mon-6) as a starting point. Based on Figure 13a we selected 1 kbar as the constant fractionation pressure. We added 3 wt. % magmatic H_2O to ensure vapor saturation. We then explored isobaric fractional crystallization at a range of fO_2 buffers. The best fit to the monzogranite suite arose at the NNO (nickel/nickel oxide) buffer. As shown by the green lines in Figures 7 and 8, this model matches almost all the major oxide and trace element trends for the monzogranite group of samples, including the gentle enrichment slopes of the trace elements, the nearly flat alkalis, and (arguably) the change in slope of Al_2O_3 vs. SiO_2 at ~71.3 wt.% SiO_2. The only notable exception is CaO, which may show a scattered negative correlation with SiO_2 among the monzogranite samples that is not captured by the fractionation model.

However, the success of this model in describing the evolution among the monzogranites evidently does not extend to the rest of the petrologic types. The parallel but offset trends evident in other rock types cannot be captured by a single liquid line of descent. It is necessary, instead, that some other process acted on the primitive end of the suite, after emplacement of the monzogranite. Hence, we began again with the most primitive syenogranite (Syen-1). We simulated isobaric fractional crystallization of this composition at the same conditions as before. As shown by the brown lines in Fig. 7 and 8, this model successfully accounts for major- and trace-element features of the syenogranite group and many features of the alkali feldspar granite group as well. Hence, samples of the second pulse of magmatism at Ad-Dayheen, like the first (monzogranite) pulse, appear to be related to one another by simple fractionation. But the starting point is offset from any liquid that occurs on the monzogranite fractionation trend and,

once again, the syenogranite fractionation path does not explain the alkaline and peralkaline granites, microgranites, or pegmatites.

At this point, we hypothesize that whatever process modified the unerupted magma after emplacement of monzogranite but before emplacement of syenogranite continued to operate in the same fashion, leading to a parental liquid for the alkaline and peralkaline granite pulse. We created a new parental model liquid by extending the composition vector from Mon-6 through Syen-1 and an equal distance beyond. The liquid line of descent of this new composition at the same fractionation conditions as above is shown by the blue lines in Figures 7 and 8. Remarkably, this model successfully reproduces many features of the alkaline granite, peralkaline granite, microgranite, and even pegmatite suites, including trends in Al_2O_3, K_2O, Na_2O, and total alkalis. It matches nearly every trace element in the alkaline and peralkaline granites and also some trace elements in microgranite and pegmatite, although these latter two types show additional enrichment in Nb, Y, Zr, Ta, Th, and U above what is predicted by the fractionation model.

The models are not perfect. They do not predict the overall increase in $Fe_2O_3^T$ in the suite or the low MgO and CaO of samples with >73 wt.% SiO_2. Possibly they could be improved with further tuning of the fO_2, H_2O, and pressure settings or by variations in these quantities along the fractionation paths. Given the absence of F in the model, however, such effort would not be justified. Yet the models appear to illustrate the essential behavior of the system quite well. The main conclusion, that all the rocks in the suite cannot be generated by fractional crystallization from a single parent, is robust despite the model shortcomings. A very important feature of this set of three parallel but offset fractionation paths is that none of the individual paths matches the overall depletion of Sr, Ba, CaO, and Eu/Eu* that characterizes the entire Ad-Dayheen magmatic

suite. This is simply because none of these models predicts sufficiently rapid fractionation of plagioclase or, alternatively, because the fractionating assemblage causes SiO_2 to increase too rapidly in the residual liquid. Instead, the dominant loss process for Sr, Ba, CaO, and Eu appears to be the hypothesized modification of the parental liquids that occurs before fractionation of each of the three magmatic pulses occurs. Just as depletion of Sr, Ba, CaO, and Eu mostly occurs between magmatic pulses rather than during fractional crystallization of each magmatic pulse, likewise rapid enrichment in Nb, Y, Rb, Zr, Ga, Ta, Th, U, and LREEs is apparent only when all magmatic types are considered together. We infer that the same process is responsible for these anomalous enrichments (except in heavily mineralized samples), whereas simple fractional crystallization can explain the more modest enrichment seen within each petrologic type.

What remains to be explored, then, is the nature of the process that caused the modification of the parental melt from primitive monzogranite to primitive syenogranite and subsequently, along the same modification vector, to primitive peralkaline granite. This process, at nearly constant SiO_2, is associated with modest depletion in TiO_2 and MgO; substantial depletion in Al_2O_3, CaO, Ba, Sr, and Eu; and substantial enrichment in Na_2O, K_2O, Zn, Rb, Ga, Nb, Zr, Y, Hf, Ta, Th, U, and REEs except Eu. In summary, the ingredients of fluorite are selectively removed while HFSEs are strongly concentrated. We suggest that the process responsible for these changes is addition of a F-rich, HFSE-bearing component. As discussed above, the data extend along the F-enrichment trend of Manning (1981), but in fact the extent of enrichment in F (from ~1% to ~4%) implied by Fig. 13a is too steep to be explained by closed system fractional crystallization, which would enrich F (like all the other incompatible elements in the suite) by at most ~50% between 70.5 and 75.0 wt.% SiO_2. Moreover, magmatic fluorite is present in all members of the suite, and so fluorine was introduced before extensive

fractionation. Lukkari and Holtz (2007) experimentally investigated the effects of F addition to granite and found a result not apparent in the Ab-Or-Q-H_2O-F study of Manning (1981), namely that increasing F concentration drives a rapid decrease in the CaO content of melts and coexisting plagioclase, driven to near zero by precipitation of fluorite. Furthermore, the very common correlation in rare-metal granites between F content and HFSE enrichment (Kovalenko, 1995; Wang et al., 2018) indicates that F-bearing components are effective agents of transport for HFSEs, due to the exceptional strength of F^- as a ligand (Keppler, 1983).

7.4. Oxygen fugacity

Alkali feldspar granite sample AFG-2 contains both magnetite and ilmenite, which offers the possibility of applying a two-oxide oxybarometer calibration to estimate temperature and oxygen fugacity. However, the magnetite in this rock is extremely low in TiO_2, 0.16±0.02 wt.% (excluding one high outlier with 0.35 wt.% TiO_2 and points with anomalously low MnO and MgO that are less likely to have equilibrated with ilmenite) and the ilmenite is both extremely rich in MnO (5.35±0.32 wt.%, excluding one high and one low outlier) and very low in hematite component. These compositions plot outside the calibrated range of published two-oxide calibrations. However, attempting to use the calibration of Sauerzapf et al. (2008) yields T ~ 600 °C and fO_2 ~ NNO+3. This result may be qualitatively interpreted to indicate either (a) that the oxide phases in alkali feldspar granite crystallized very late in the petrogenesis, from an oxidized, low-temperature, residual melt or (b) that the oxide phases re-equilibrated in the subsolidus, leading to a nearly complete loss of TiO_2 from the magnetite and significant loss of Fe_2O_3 from the ilmenite.

A more promising avenue to constraining magmatic fO_2 during differentiation lies in the biotite composition in syenogranite. As explored by Bucholz et al. (2018) and references therein,

the annite content of biotite is sensitive to fO_2, once other variables such as temperature and whole rock Fe/Mg are accounted for, which can be done with the MELTS model. The mean Fe/(Fe+Mg) = 0.58 ± 0.02 in biotite in sample Syen-3 is consistent, according to MELTS, with fO_2 ~ 1.5 log units below the NNO buffer, which is somewhat more reducing than the liquid lines of descent that best fits the major element trends in the suite, suggesting some internal inconsistency in the use of MELTS to define magmatic fO_2 in this suite. This may be an effect, for example, of the absence of F in the MELTS model calculations, which causes biotite to crystallize at a different temperature than it would have in the natural syenogranite.

7.4. Origin of the snowball texture

Quartz grains in the alkali feldspar granite samples display a distinctive snowball texture. This texture may be an important petrogenetic indicator. Snowball textures have been variously attributed to both magmatic (e.g., Kovalenko, 1995; Müller and Seltmann, 1999; Li et al., 2000) and metasomatic processes (Müller and Seltmann, 1999; Wu et al., 2018). Under fluid-enriched conditions, quartz crystals grow rapidly, overtaking and enclosing slower-growing albite crystals (Müller and Seltmann, 1999; Li et al., 2000). Müller and Seltmann (1999) go further and claim that it is a unique indicator of growth from a fluid-saturated melt enriched in F and Li. Li et al. (2000), however, concluded that F is not essential for the formation of snowball quartz, even though snowball quartz is more common in high-F granites.

Snowball texture, similar to that seen at Ad-Dayheen, is observed also in the Mueilha and Nuweibi intrusions in the Eastern Desert of Egypt. Azer et al. (2019) and Seddik et al. (2020) attributed the presence of snowball texture in these two occurrences to magmatic origins, citing numerous lines of evidence. Similar arguments apply in the Ad-Dayheen case, including: (1) the snowball quartz crystals are subhedral to euhedral and of uniform size; (2) there are rare

inclusions of biotite within the snowball quartz; (3) flow-aligned albite is found in both the groundmass and in snowball quartz phenocrysts; (4) the albite crystals included in snowball quartz have euhedral to subhedral habit and concentric arrangement; and (5) no fractures are observed within the snowball quartz, whereas replacement of quartz by albite can obviously not be a closed-system transformation. We conclude that snowball quartz is a magmatic feature of the Ad-Dayheen intrusion.

7.5. Geodynamic model: post-collisional lithospheric delamination

Post-collisional alkaline/peralkaline granitoids are widely distributed in the Arabian Shield and may also be a significant component of less well-preserved and exposed continental terranes. Therefore, understanding the origin of these rocks has significant geodynamic implications. The abundance and wide distribution of such granitoids likely attests to the high growth rate and elevated geotherm in the shield during the collisional phase and cannot be explained solely by simple arc-arc accretion models (e.g. Stein and Hofmann, 1994). Some authors have suggested that the high crustal growth rates in the ANS were driven by asthenospheric upwelling, perhaps during the collisional stage due to a component of oblique convergence and orogen-parallel extension (Katz et al. 2004) or afterwards due to lithospheric delamination (e.g., Avigad and Gvirtzman, 2009). The lithospheric delamination model for post-collisional ANS magmatism has been adopted by many authors (e.g., Avigad and Gvirtzman, 2009; Farahat and Azer, 2011).

At the end of the collisional stage, the crust was moderately thickened and the lithospheric mantle was significantly thickened. Geodynamic models suggest that, with the end of convergence, the Mozambique ocean slab may have broken off, setting up a downwelling convergent flow that imposed a downward traction on the overlying lithosphere that may have

triggered its delamination. Subsequent removal of the negative buoyancy of the slab, together with replacement of cold lithosphere by buoyant asthenosphere, led to major isostatic uplift, inducing in turn upper crustal erosion. Both input of heat from the asthenosphere and elevation of the geotherm by rapid unroofing can drive partial melting of metasomatized lithospheric mantle and lower continental crust. In the present case, it is difficult to trace any material contribution from mantle-derived mafic magma (though mantle-derived fluids are a possible source of F and HFSEs), so we prefer a scenario in which felsic magma was directly generated by melting of lower crust. Each pulse of primary magma experienced assimilation of a F-bearing component, ascent to upper crustal levels, fractional crystallization, and emplacement at ≤0.1 GPa pressure (~3 km) depth. Water and fluorine were likely present early in the process, by the time the magma had evolved to monzogranite composition, but addition continued as magma was stored between pulses of upper-crustal emplacement. Shear zones and large-scale intra-continental faults may have facilitated migration of mantle-derived volatiles into hot crustal source regions. This would account for the clustering of post-collisional alkaline magmatism along sutures and shear zones throughout the northern ANS. The common occurrence of strike-slip faults, core complexes, dike swarms and shear zones attest to an extensional stress regime during the post-collisional stage of ANS evolution (Blasband et al., 2000).

7.6. Evolution of mineralization

Mineralization of the Ad-Dayheen intrusion was cogenetic with the emplacement of the intrusion itself, associated with high-temperature late magmatic to early hydrothermal processes. We do not find evidence for significant younger modification or epithermal enrichment. Several studies have investigated the processes whereby rare metals reach economic concentrations in A-type rocks (e.g., Gysi and Williams-Jones, 2013; Möller and Williams-Jones, 2016; Vasyukova

et al., 2016). The main hypotheses include: 1) magmatic source and process, with concentration reflecting incompatibility of the rare metals and extreme fractional crystallization (Kovalenko, 1995); 2) magmatic source and a combination of magmatic and hydrothermal processes, wherein HFSE and REE preconcentrated into residual melt were remobilized and further concentrated to economic grade by hydrothermal fluid migration (Salvi and Williams-Jones, 1996; Gysi and Williams-Jones, 2013); and 3) fluoride-silicate melt immiscibility, whereby LREE partitioned into fluoride melt while HFSE were enriched in coexisting silicate melt (Vasyukova et al., 2016). It has proven challenging in many cases to distinguish among models because most rare-metal alkaline granites are associated with intense post-magmatic alteration that obscures magmatic and early hydrothermal mineral assemblages (Salvi and Williams-Jones, 1996). In this regard, the Ad-Dayheen intrusion is exceptional. Mineral assemblages reflecting late-magmatic to early-hydrothermal stages are preserved, offering an opportunity for understanding primary enrichment mechanisms that are commonly erased in similar deposits. The positive correlations among geochemically coherent elements Zr-Hf, Nb-Ta, and Y-Ho (Fig. 13) suggest that magmatic enrichment of these elements remained largely unmodified by later processes.

Although we do observe subsolidus re-equilibration textures and formation of secondary minerals at the expense of K-feldspar in the alkaline/peralkaline granites and pegmatite, a magmatic origin for the hydrothermal solutions that affected these granites is favored. This is supported by the presence of pegmatite at the outer margins of alkaline/peralkaline granites and by the gradational boundaries of these pegmatites. Extended fractional crystallization in the Dayheen granites eventually produced a saturated, late-magmatic, F-bearing fluid. This fluid migrated towards the apex of the magma chamber, reacting with still hot but subsolidus granite

and becoming increasingly focused into distinct channels and veins. This upward and outward mode of fluid migration led to pegmatites with gradational boundaries.

Mineralization of the Ad-Dayheen intrusion is mainly concentrated in the peralkaline granite, microgranite and pegmatite. Textural and mineralogical patterns reveal two main stages of mineralization. The early stage is preserved in early-crystallizing magmatic phases such as fergusonite, gadolinite, and zircon. The late stage is shown by alteration and partial replacement of the magmatic phases as well as neoblastic growth of phases such as pyrochlore, bastnaesite, secondary zircon and xenotime. In the microgranite and pegmatites, for example, fergusonite is zoned and replaced by pyrochlore. Bastnaesite occurs exclusively as veinlets associated with gadolinite in the quartz veins.

Zircon morphology can be used to study changes in crystallization environment (Corfu et al., 2003). Magmatic zircon commonly displays prismatic shapes, oscillatory zoning, and intergranular textures (Corfu et al., 2003). Most zircons in the early phases of the Ad-Dayheen intrusion (monzogranite, syenogranite, alkali feldspar granite and alkaline/peralkaline granite) satisfy these criteria, forming prismatic crystals with oscillatory zoning. On the other hand, most zircons in the microgranite and pegmatite are anhedral to subhedral equant crystals, unzoned or showing patchy zoning, and have a spongy texture with abundant fluid and mineral inclusions. These are characteristic features of hydrothermal zircon or magmatic zircon that has undergone interaction with a fluid phase (Corfu et al., 2003). Also, during the hydrothermal stage, zircon continued to crystallize in pegmatite, replacing aegirine or as aggregates associated with hematite and bastnaesite. The crystallization of acicular aegirine in the pegmatite records the transition between magmatic and hydrothermal environments; later hematization of aegirine took place during the hydrothermal stage.

Summary

The Ad-Dayheen intrusion is typical in many ways of the post-collisional, mineralized A-type granitoid ring complexes of late Neoproterozoic age (613-625 Ma) in the Arabian Shield. Field relationships enable the recognition of three pulses of magmatic activity in the Ad-Dayheen intrusion. The first phase formed a core of monzogranite. The second phase formed a ring of syenogranite, alkali feldspar granite, and microgranite. The third phase of alkaline/peralkaline granite and pegmatite crosscuts the second phase rocks. Separation of fluids from the oversaturated melt promoted segregation and emplacement of pegmatite and veins of fluorite and quartz as the magmatic stage transitioned into an early hydrothermal stage.

All the granitoids of the Ad-Dayheen intrusion are highly evolved leucocratic granites, alkaline to peralkaline in character, with geochemical characteristics typical of within-plate tectonic environments and A-type granites. They contain sodic amphibole and aegirine; high concentrations of Na_2O+K_2O, Fe_2O_3, Nb, Ta, Zr Y, and REE; and low concentrations of CaO, Al_2O_3, Ba and Sr. They exhibit pronounced negative Eu anomalies (Eu/Eu* = 0.11-0.35). Each pulse of the Ad-Dayheen intrusion defines coherent and cogenetic geochemical signatures, but they cannot all be related to one another by simple fractional crystallization; other open-system processes are required.

The Ad-Dayheen case is consistent with the general geodynamic model for post-collisional magmatism in the ANS in which lithospheric delamination drove delivery of hot asthenospheric material to the base of an uplifted crust. Transfer of mantle-derived heat and fluids led to partial melting of the juvenile lower crustal material and ascent of melts along strike-slip faults, shear zones, and oblique extensional structures. Assimilation of a F-rich component drove shifts in the composition of stored magma between the three pulses of activity.

Each pulse of ascending magma underwent fractional crystallization, generating a set of subparallel compositional trends in the overall intrusive suite. Elements incompatible in the early fractionating phases, such as REE (except Eu) and HFSE, became concentrated in residual melt, along with H_2O and F, leading eventually to exsolution of a fluid phase and precipitation of REE- and HFSE-rich accessory minerals.

Mineralization is abundant in microgranite and pegmatite outcrops and, to a lesser extent, in peralkaline granite. The evidence suggests that mineralization was cogenetic with their actual intrusion, reflecting both magmatic enrichment and early hydrothermal mobilization of metals originally present in the primary melt. The residual volatile-rich fraction of alkali granite magma was dominantly emplaced as a subvolcanic microgranite in the chilled carapace at the apex of the intrusion. The hydrothermal stage was characterized by alteration of sodic amphibole with formation of secondary zircon, monazite and xenotime; by alteration of fergusonite to pyrochlore; and by crystallization of bastnaesite as veinlets in the late gadolinite. Although the present study is not an assessment of the resource potential of the area, the high concentrations of strategic metals that we have recorded suggests that such as assessment is a priority for future work.

Acknowledgements

The authors would like to extend their appreciation and gratitude to the King Saud University for funding and supporting this work through Researchers Supporting Project number (RSP-2020/151), King Saud University, Riyadh, Saudi Arabia. PDA is supported by the US NSF award EAR-1826310.

Declaration of interests

The authors declare that they have no known competing financial interests or personal relationships that could have appeared to influence the work reported in this paper.

References

Abdallah, S.E., Azer, M.K., El Shammari, A.S., 2020. Petrological and geochemical evolution of Ediacaran rare-metal bearing A-type granites from Jabal Aja complex, northern Arabian Shield, Saudi Arabia. Acta Geologica Sinica 94(3), 743-762.

Abdel-Rahman, A.M., 1994. Nature of biotites from alkaline, calc-alkaline and peraluminous magmas. Journal of petrology 35, 525-541.

Abuamarah, B.A., 2020. Genesis and petrology of postcollisional rare-metal-bearing granites in the Arabian Shield: A case study of Aja ring complex, northern Saudi Arabia. The Journal of Geology 128, 131–156.

Abuamarah, B.A., Azer, M.K., Asimow, P.D., Ghrefat, H., Mubarak, H.S., 2020. Geochemistry and Petrogenesis of late Ediacaran Rare-metal Albite Granites of the Arabian-Nubian Shield. Acta Geologica Sinica (Published online: doi:10.1111/1755-6724.14379).

Ali, K.A., Jeon, H., Andresen, A., Li, S.Q., Harbi, H.M., Hegner, E., 2014. U–Pb zircon geochronology and Nd–Hf–O isotopic systematics of the Neoproterozoic Hadb adh Dayheen ring complex, central Arabian Shield, Saudi Arabia. Lithos 206, 348-360.

Avigad, D., Gvirtzman, Z., 2009. Late Neoproterozoic rise and fall of the northern Arabian–Nubian shield: the role of lithospheric mantle delamination and subsequent thermal subsidence. Tectonophysics 477, 217–228.

Azer, M.K., 2013. Late Ediacaran (605–580 Ma) post-collisional alkaline magmatism in the Arabian–Nubian Shield: a case study of Serbal ring-shaped intrusion, southern Sinai, Egypt. Journal of Asian Earth Sciences 77, 203-223.

Azer, M.K., Abdelfadil, K.M. and Ramadan, A.A., 2019. Geochemistry and Petrogenesis of Late Ediacaran Rare-Metal Albite Granite of the Nubian Shield: Case Study of Nuweibi Intrusion, Eastern Desert, Egypt. The Journal of Geology 127(6), 665-689.

Azer, M.K., Obeid, M.A., Ren, M., 2014. Geochemistry and petrogenesis of late Ediacaran (580-605 Ma) post-collisional alkaline rocks from Katherina Ring complex, south Sinai., Egypt. Journal of Asian Earth Sciences 93, 229-252.

Batchelor, R.A., Bowden, P., 1985. Petrogenetic interpretation of granitoid rock series using multicationic parameters. Chemical Geology 48, 43-45.

Be'eri-Shlevin, Y., Katzir, Y., Whitehouse M., 2009. Post-collisional tectono-magmatic evolution in the northern Arabian-Nubian Shield (ANS): Time constraints from ion-probe U-Pb dating of zircon. Journal of Geological Society of London 166, 71-85.

Blasband, B., White, S., Brooijmans, P., De Broorder, H., Visser, W., 2000. Late Proterozoic extensional collapse in the Arabian-Nubian Shield. Journal of Geological Society of London 157, 615–628.

Bucholz, C. E., Stolper, E. M., Eiler, J. M., Breaks, F. W., 2018. A Comparison of Oxygen Fugacities of Strongly Peraluminous Granites across the Archean–Proterozoic Boundary, Journal of Petrology 59, 2123–2156.

Corfu, F., Hanchar, J.M., Hoskin, P.W.O., Kinny, P., 2003. Atlas of zircon textures. Reviews in Mineralogy and Geochemistry 53, 469–500.

Cuney, M., Marignac, C., Weisbrod, A., 1992. The Beauvoir topaz-lepidolite albite granite (Massif Central France): the disseminated magmatic Sn–Li–Ta–Nb–Be mineralization. Economic Geology 87, 1766–1794.

Davidson, J.P., Dungan, M.A., Ferguson, K.M., Colucci, M.T., 1988. Crust-magma interactions and the evolution of arc magmas: the San Pedro-Pellado Volcanic Complex Southern Chilean Andes. Geology 15, 443-446.

De la Roche, H., Leterrier, J., Grandclaude, P., Marchal, M., 1980. A classification of volcanic and plutonic rocks using R_1-R_2 diagrams and major-element analyses-Its relation with current nomenclature. Chemical Geology 29, 183-210.

Dingwell, D.B. 1985. The structure and properties of fluorine-rich silicate melts: implications for granite petrogenesis. In R.P. Taylor and D.F. Strong (eds.), Granite-related mineral deposits geology, petrogenesis and tectonic setting, CIM Conference on Granite-related Mineral Deposits, 72-81.

Drysdall, A.R., Douch, C.J., 1986. Nb–Th–Zr mineralization in microgranite – microsyenite at Jabal Tawlah, Midyan region, Kingdom of Saudi Arabia. Journal of African Earth Sciences 4, 275–288.

Eby, G.N., 1992. Chemical subdivisions of the A-type granitoids: petrogenesis and tectonic implications. Geology 20, 641-644.

Evensen, N.M., Hamilton, P.J., O' Nions, R.K., 1978. Rare earth abundances in chondritic meteorites. Geochimica et Cosmochimica Acta 42(8), 1199-1212.

Eyal, M., Litvinovsky, B., Jahn, B.M., Zanvilevich, A., Katzir Y., 2010. Origin and evolution of post-collisional magmatism: Coeval Neoproterozoic calc-alkaline and alkaline suites of the Sinai Peninsula. Chemical Geology 269, 153-179.

Farahat, E.S., Azer, M.K., 2011. Post-collisional magmatism in the northern Arabian-Nubian Shield: the geotectonic evolution of the alkaline suite at Gebel Tarbush area, south Sinai, Egypt. Chemie der Erde 71, 247-266.

Genna, A., Nehlig, P., Le Goff, E., Guerrot, C., Shanti, M., 2002. Proterozoic tectonism of the Arabian Shield. Precambrian Research 117, 21–40

Girardeau, J., Mevel, C., 1982. Amphibolitized sheared gabbros from ophiolites as indicators of the evolution of the oceanic crust: Bay of islands, Newfoundland. Earth and Planetary Science Letters 61, 151-165.

Gualda, G. A. R., Ghiorso, M. S., Lemons, R. V., Carley, T. L., 2012. Rhyolite-MELTS: A Modified Calibration of MELTS Optimized for Silica-Rich, Fluid-Bearing Magmatic Systems. Journal of Petrology 53, 875–90.

Gysi, A.P., Williams-Jones, A.E., 2013. Hydrothermal mobilization of pegmatite-hosted REE and Zr at Strange Lake, Canada: A reaction path model. Geochimica et Cosmochimica Acta 122, 324–352.

Hannah, J.L. and Stein, H.J. 1990. Magmatic and hydrothermal processes in ore bearing systems. In H.J. Stein and J.L. Hannah (eds.), Ore-bearing granite systems; petrogenesis and mineralizing processes. Geological Society of America, Special Paper, 246, 1-10.

Hargrove, U.S., Stern, R.J., Kimura, J.-I., Manton, W.I., Johnson, P.R., 2006. How juvenile is the Arabian-Nubian Shield? Evidence from Nd isotopes and pre-Neoproterozoic inherited zircon in Bi'r Umk suture zone, Saudi Arabia. Earth and Planetary Science Letters 252, 308-326.

Harris, N.B.W., 1985. Alkaline complexes from the Arabian Shield. Journal of African Earth Sciences 3, 83–88.

Hawthorne, F.C., Oberti, R., Harlow, G.E., Maresch, W.V., Martin, R.F., Schumacher, J.C., Welch, M.D., 2012. IMA report, nomenclature of the amphibole supergroup. American Mineralogist, 97, 2031-2048.

Jarrar, G.H., Manton, W.I., Stern, R.J., Zachmann F., 2008. Late Neoproterozoic A-type granites in the northernmost Arabian-Nubian Shield formed by fractionation of basaltic melts. Chemie der Erde 68, 295-312.

Johnson, P.R., Kattan, F.K. (2012) The geology of the Arabian Shield. A review of the geology of Precambrian rocks, Kingdom of Saudi Arabia. SGS, Special Publication, Riyadh.

Katz, O., Beyth, M., Miller, N., Stern, R., Avigad, D., Basu, A., Anbar, A., 2004. A Late Neoproterozoic (630 Ma) Boninitic Suite from southern Israel: implications for the consolidation of Gondwanaland. Earth and Planetary Science Letters 218, 475–490.

Keppler, H., 1993. Influence of fluorine on the enrichment of high field strength trace elements in granitic rocks. Contributions to Mineralogy and Petrology 114, 479-488.

King, P.L., White, A.J.R., Chappel, B.W., Allen, C.M., 1997. Characterization and origin of aluminous A-type granites from the Lachlan Fold Belt, southeastern Australia. Journal of Petrology 38, 371–391.

Kovalenko, V.I., 1995. The peralkaline granite-related Khaldzan-Buregtey rare metal (Zr, Nb, REE) deposit, western Mongolia. Economic Geology 90, 530–547.

Küster, D., 2009. Granitoid-hosted Ta mineralization in the Arabian–Nubian Shield: ore deposit types, tectono-metallogenetic setting, and petrogenetic framework. Ore Geology Reviews 35, 68–86.

Lee, S.-G., Asahara, Y., Tanaka, T., Lee, S.R., Lee, T., 2013. Geochemical significance of the Rb–Sr, La–Ce and Sm–Nd isotope systems in A-type rocks with REE tetrad patterns and negative Eu and Ce anomalies: The Cretaceous Muamsa and Weolaksan granites, South Korea. Chemie der Erde –Geochemistry 73, 75-88.

Li, F. C., Zhu, J. C., Jin, Z. D., Li, X. F., 2000. Formation mechanism of snowball texture in albite granite. Acta Petrologica et Mineralogica 19, 27-35.

Liégeois, J.P., Black, R., 1987. Alkaline magmatism subsequent to collision in the Pan-African belt of the Adrar des Iforas. In: Fitton, J.G., Upton, B.G.J. (Eds.), Alkaline Igneous Rocks. Geological Society, Special Publication 30, 381-401.

Liégeois, J.P., Navez, J., Black, R., Hertogen, J., 1998. Contrasting origin of post-collision high-K calc-alkaline and shoshonitic versus alkaline and peralkaline granitoids. The use of sliding normalization. Lithos 45, 1-28.

Locock, A.J., 2014, An Excel spreadsheet to classify chemical analyses of amphiboles following the IMA 2012 recommendations, Computers & Geosciences, 62, 1-11.

London, D., Hervig, R.L., Morgan, G.B., 1988 Melt-vapor solubilities and elemental partitioning in peraluminous granite-pegmatite systems: experimental results with Macusani glass at 200 MPa. Contribution to Mineralogy and Petrology 99, 360–373.

Lukkari, S., Holtz, F., 2007. Phase relations of a F-enriched peraluminous granite: an experimental study of the Kymi topaz granite stock, southern Finland. Contributions to Mineralogy and Petrology 153, 273-288.

Manning, D.A.C., 1981. The effect of fluorine on liquidus phase relationships in the system Qz–Ab–Or with excess water at 1 kb. Contributions to Mineralogy and Petrology76, 206–215.

Moghazi, A.M., Harbi, H.M., Ali, K.A., 2011. Geochemistry of the Late Neoproterozoic Hadb adh Dayheen ring complex, Central Arabian Shield: Implications for the origin of rare-metal-bearing post-orogenic A-type granites. Journal of Asian Earth Sciences 42(6), 1324-1340.

Möller, V., Williams-Jones, A.E., 2016. Petrogenesis of the Nechalacho Layered Suite, Canada: Magmatic evolution of a REE–Nb-rich nepheline syenite intrusion. Journal of Petrology 57, 229–276.

Moore, W.J., 1984. Mineral Potential of Felsic Plutonic Rocks in the Northern Central Arabian Shield, Kingdom of Saudi Arabia. Saudi Arabian Deputy Ministry for Mineral Resources Open – File Report USGS 04-44, 44 p.

Morag, N., Avigad, D., Gerdes, A., Belousova, E., Harlavan, Y., 2011. Crustal evolution and recycling in the northern Arabian-Nubian Shield: New perspectives from zircon Lu–Hf and U–Pb systematics. Precambrian Research 186, 101–116.

Morimoto, N., Fabries, J., Ferguson, A.K., Ginzburg, I.V., Ross, M., Seifert, F.A., Zussman, J., 1988. Nomenclature of pyroxenes. Mineralogical Magazine 52, 535–550.

Moufti, A.M., Ali, K.A., Whitehouse, M.J., 2013. Geochemistry and petrogenesis of the Ediacaran post-collisional Jabal Al-Hassir ring complex, Southern Arabian Shield, Saudi Arabia. Geochemistry 73(4), 451-67.

Muller, A., Seltmann, R., 1999. The genetic significance of snowball quartz in high fractionated tin granites of the Krusne Hory / Erzgebirge. Mineral deposits: processes to processing 1, 409-12.

Mushkin, A., Navon, O., Halicz, L., Heimann, A., Hartmann, G., Stein, M., 2003. The petrogenesis of A-type magmas from the Amram Massif, southern Israel. Journal of Petrology 44, 815–832.

Nachit, H., Ibhi, A. and Ohoud, M.B., 2005. Discrimination between primary magmatic biotites, reequilibrated biotites and neoformed biotites. Comptes Rendus Geoscience, 337(16), pp.1415-1420.

Nachit, H., Razafimahefa, N., Stussi, J.M., Carron, J.P., 1985. Composition chimique des biotites et typologie magmatique des granitoides. Comptes Rendus Hebdomadaires de l'Academie des sciences 301(11), 813-818.

Nurmi, P.A., Haapala, I., 1986. The Proterozoic granitoids of Finland: granite types, metallogeny and relation to crustal evolution. Bulletin of the Geological Society of Finland 58, 203-233.

Pearce, J.A., 1983. Role of the sub-continental lithosphere in magma genesis at active continental margins. In: Hawkesworth, C.J., Norry, M.J. (Eds.), Continental Basalts and Mantle Xenoliths. Shiva, Nantwich, pp. 230-249.

Pearce, J.A., Harris, N.B.W., Tindle, A.G., 1984. Trace element discrimination diagrams for the tectonic interpretation of granitic rocks. Journal of Petrology 25, 956-983.

Pe-Piper, G., (2007). Relationship of amphibole composition to host-rock geochemistry: the A-type gabbro-granite Wentworth pluton, Cobequid shear zone, eastern Canada. European Journal of Mineralogy 19(1), 29-38.

Salvi, S., Williams-Jones, A.E., 1996. The role of hydrothermal processes in concentrating high-field strength elements in the Strange Lake peralkaline complex, northeastern Canada. Geochimica et Cosmochimica Acta 60, 1917–1932.

Samuel, M.D., Moussa, H.E., Azer, M.K., 2007. A-type volcanics in central eastern Sinai, Egypt. Journal of African Earth Sciences 47(4-5), 203-226.

Sauerzapf, U., Lattard, D., Burchard, M., Engelmann, R., 2008. The Titanomagnetite–Ilmenite Equilibrium: New Experimental Data and Thermo-oxybarometric Application to the Crystallization of Basic to Intermediate Rocks. Journal of Petrology 49, 1161–1185.

Seddik, A.M., Darwish, M.H., Azer, M.K. and Asimow, P.D., 2020. Assessment of magmatic versus post-magmatic processes in the Mueilha rare-metal granite, Eastern Desert of Egypt, Arabian-Nubian Shield. Lithos, p.105542.

Shang, C.K., Morteani, G., Satir, M., Taubald, H., 2010. Neoproterozoic continental growth prior to Gondwana assembly: constraints from zircon–titanite geochronology, geochemistry and petrography of ring complex granitoids, Sudan. Lithos 118, 61–81

Smith, P. M. and Asimow, P. D., 2005. Adiabat_1ph: A New Public Front-End to the MELTS, PMELTS, and PHMELTS Models. Geochemistry Geophysics Geosystems 6, Q02004.

Stein, M., Hofmann, A.W., 1994. Mantle plumes and episodic crustal growth. *Nature* 372, 63-68.

Stern, R.J., Johnson, P.R., 2010. Continental lithosphere of the Arabian Plate: A geologic, petrologic, and geophysical synthesis. Earth Science Review 101, 29-67.

Sylvester, P.J., 1989. Post-collisional alkaline granites. Journal of Geology 97(3), 261-280.

Valley, J.W., Kinny, P.D., Schulze, D.J., Spicuzza, M.J., 1998. Zircon megacrysts from kimberlite: oxygen isotope variability among mantle melts. Contribution to Mineralogy and Petrology 133, 1–11.

Vasyukova, O. V., Williams-Jones, A.E., Blamey, N.J.F.F., 2016. Fluid evolution in the Strange Lake granitic pluton, Canada: Implications for HFSE mobilisation. Chemical Geology 444, 83–100.

Wang, L.-X., Ma, C.-Q., Zhang, C., Zhu, Y.-X., Marks, M. A. W., 2018. Halogen geochemistry of I- and A-type granites from Jiuhuashan region (South China): Insights into the elevated fluorine in A-type granite, Chemical Geology 478:164-182.

Whalen, J.B., Currie, K.L., Chappell, B.W., 1987. A-type granites: geochemical characteristics, discrimination and petrogenesis. Contribution to Mineralogy and Petrology 95(4), 407-419.

Winkler, H.G.F., Boese, M., Marcopoulos, T., 1975. Low temperature granite melts. Neues Jahrbuch für Mineralogie. Monatshefte 6, 245–268.

Wu, F.-Y., Sun, D.-y., Li, H., Jahn, B.-M., Wilde, S., 2002. A-type granites in northeastern China: age and geochemical constraints on their petrogenesis. Chemical Geology 187, 143–173.

Wu, M., Tian, B., Zhang, D., Xu, G., Xu, W., Qiu, K., 2018. Zircon of the No. 782 deposit from the Great Xing'an Range in NE China: Implications for Nb-REE-Zr mineralization during magmatic-hydrothermal evolution. Ore Geology Reviews 102, 284–299.

Figure Captions

Figure 1. Simplified geologic map of the Arabian Shield in Saudi Arabia (modified after Stern and Johnson, 2010), indicating the distribution of major features such as suture zones, basins, ophiolites, faults, and terrane boundaries. The distribution of alkaline/peralkaline granites and ring complexes is shown in red. The location of Hadhb't Ad-Dayheen is indicated.

Figure 2. Geological map of the Ad-Dayheen intrusion, showing the different rock units and major faults (modified after Moghazi et al., 2011; Ali et al., 2014).

Figure 3. Field photographs showing (a) a roof-pendant of alkali feldspar granite above peralkaline granite, (b) microgranite appears intruding the alkali feldspar granite, and (c) a thin layer of pegmatite. The person is the scale for the three field photos.

Figure 4. Photomicrographs showing petrographic textures in cross-polarized transmitted light (c, l), plane-polarized transmitted light (a, h, i, j, k, m, n), or back-scattered electron intensity (b, d, e, f): (a) crystals of biotite in monzogranite, (b) inclusions of apatite in albite in the alkali feldspar granite, (c) snowball texture in the alkali feldspar granite, (d) prismatic crystals of aegirine in alkaline granite, (e) inclusion of monazite within aegirine in peralkaline granite, (f) zircon and quartz inclusions in arfvedsonite, (g) secondary zircons associated with monazite, (h) allanite associated with altered mafic minerals, (i) riebeckite in microgranite, (j) arfvedsonite in microgranite, (κ) xenotime in microgranite, (l) arfvedsonite in pegmatite, (m) riebeckite containing zircon inclusions in pegmatite, and (n) a fergusonite crystal in pegmatite. The mineral abbreviations are: Qz = quartz , Ab = albite, Arf = arfvedsonite, Kfs = K-feldspar, Bt = biotite, Aeg = aegirine, Rbk = riebeckite, Xtm = xenotime, Frg = Fergusonite, Fl = fluorite, Aln = allanite, Mnz = monazite, Zrn = zircon, and Ap = apatite.

Figure 5. Classification diagrams based in mineral chemistry: (a) clinopyroxene classification after Morimoto et al. (1988), (b) biotite in syenogranite classified using the $10*TiO_2$-(FeO^T+MnO)-MgO diagram of Nachit et al. (2005), (c) FeO^T vs. Al_2O_3 biotite discriminant diagram (Abdel-Rahman, 1994), (d) Na_2O vs. FeO diagram for amphiboles after Pe-Piper (2007).

Figure 6. Petrological classification of Ad-Dayheen granitoids using the R_1-R_2 diagram of De la Roche et al. (1980).

Figure 7. Silica variation diagrams of some major oxides for the different rock types of the Ad-Dayheen intrusion; pegmatite analyses may go off scale in some cases (all axis scales in weight %). Three fractional crystallization trends calculated by rhyoliteMELTS are

indicated, beginning from the most primitive monzogranite, the most primitive syenogranite, and from a hypothetical primitive peralkaline granite (see text).

Figure 8. Silica variation diagrams of some trace elements for the different rock types of the Ad-Dayheen intrusion; pegmatite analyses may go off-scale in some diagrams (SiO_2 in weight %, all trace elements in μg/g). Symbols and fractionation models as in Figure 7.

Figure 9. (a) Primitive mantle-normalized spider diagrams of the averages of the different rock types of the Ad-Dayheen intrusion and (b) chondrite-normalized REE patterns for the granitic rocks of the Ad-Dayheen intrusion. Normalization values in (a) from Pearce (1983) and in (b) from Evensen et al. (1978). Symbols as in Figure 6.

Figure 10. Whole-rock geochemical discrimination diagrams: (a) discrimination diagram of Sylvester (1989) for rocks with > 68 wt. % SiO_2, (b) Ga/Al vs. FeO/MgO diagram of Whalen et al. (1987), (c) Nb–Y–3*Ga ternary diagram (Eby, 1992), (c) Nb-Y-Ce discrimination diagram of Eby (1992), and (d) Rb/Nb vs. Y/Nb diagram for distinction of A-type granitoids (Eby, 1992). A1 = A-type granitoids with an OIB-type source, A2 = A-type granitoids with crustal sources.

Figure 11. Additional whole-rock tectonic discrimination diagrams: (a) Y+Nb vs. Rb (Pearce et al., 1984), and (b) R_1–R_2 diagram of Batchelor and Bowden (1985). Symbols as in Figure 6.

Figure 12. Indicators of magmatic evolution: (a) Rb vs. K/Rb, (b) Eu anomaly vs. Sr concentration, (c) Eu anomaly vs. CaO, and (d) Eu anomaly vs. Nb concentration. Symbols as in Figure 6.

Figure 13. (a) Normative composition of the Ad-Dayheen samples plotted in the Qz–Ab–Or projection. Dashed lines show quartz-alkali feldspar cotectics and the trace of the water-

saturated minimum melt compositions in the haplogranite system at total pressure ranging from 0.5 to 10 kbar (Winkler et al. 1975). Solid cyan line shows the trace of the minimum melt composition at 1 kbar with excess H_2O and increasing fluorine (F) content up to 4 wt.% F (Manning 1981). Additional panels show bivariate trace-element concentrations that indicate coherence of the magmatic suite: (b) Zr vs. Ga, (c) Nb vs. Ta, and (d) Y vs. Ho. Symbols as in Figure 6.

Table 1. Major and trace element contents of the granitic rocks of Ad-Dayheen intrusion.

	Monzogranite						Syenogranite				Alkali feldspar granite			Alkaline granite		
Sample	Mon-1	Mon-2	Mon-3	Mon-4	Mon-5	Mon-6	Syen-1	Syen-2	Syen-3	Syen-4	AFG-1	AFG-2	AFG-3	AG-7	AG-8	AG-9
SiO2	70.82	71.04	71.67	71.63	70.92	70.61	70.66	72.57	71.05	71.35	72.63	72.25	72.7	71.48	71.12	72.86
TiO2	0.31	0.28	0.31	0.27	0.29	0.32	0.26	0.23	0.25	0.26	0.21	0.15	0.17	0.19	0.21	0.19
Al2O3	13.31	13.51	13.29	13.43	13.51	13.27	13.07	13.04	13.47	12.98	12.18	12.56	12.99	12.56	12.66	12.23
Fe2O3	2.86	2.67	3.02	2.42	2.37	3.03	2.73	2.46	2.38	2.82	2.62	2.75	2.69	2.69	2.85	2.42
MnO	0.06	0.05	0.04	0.04	0.03	0.03	0.04	0.05	0.08	0.05	0.04	0.02	0.03	0.05	0.07	0.04
MgO	0.33	0.36	0.31	0.34	0.41	0.4	0.32	0.31	0.27	0.29	0.31	0.26	0.24	0.39	0.39	0.28
CaO	1.01	0.97	1.03	0.86	0.89	1.05	0.82	0.74	0.78	0.81	0.93	0.79	0.64	0.67	0.71	0.56
Na2O	4.58	4.43	4.36	4.44	4.69	4.58	4.95	4.81	5.17	4.82	5.06	5.02	4.89	5.84	6.22	5.65
K2O	4.76	4.66	4.58	4.73	4.87	4.62	4.85	4.73	4.65	4.66	4.86	4.47	4.73	4.67	4.58	4.42
P2O5	0.08	0.07	0.05	0.06	0.04	0.05	0.06	0.06	0.08	0.04	0.03	0.02	0.02	0.06	0.05	0.04
LOI	1.25	0.98	0.59	0.87	1.21	1.07	1.73	0.95	1.31	1.21	0.94	0.78	0.65	0.55	0.71	0.9
Total	100.06	99.02	99.25	99.09	99.77	99.23	99.53	100.15	99.51	99.29	99.81	99.07	99.75	99.5	100.09	99.79
Ni	9.8	6.1	6.2	5.6	8.7	8.9	4.5	5.7	6.2	5.6	1.9	2.1	1.4	3.1	4.6	4.8
Co	6.4	5.2	3.7	4.6	5.2	4.7	1.8	4.3	3.9	7	0.8	1.1	0.9	5.4	5.2	5.7
Sc	2.6	2.1	1.7	1.3	2.4	3.2	4.2	5.2	3.2	2.5	1.2	0.7	1.1	2.2	2.2	1.5
V	34.2	29.6	31.3	20.8	23.1	31.1	35.8	34.2	31.3	13	2.7	2.5	2.7	19.3	13.4	11.1
Cu	36.7	42.4	25.6	31.5	22.3	9.3	4.4	12.4	10.4	8.9	3.1	6.5	2.2	13.2	7.7	20.1
Pb	24.2	14.9	17.4	11.5	9.1	10.9	20.3	30.2	12.6	11	10.6	20.8	18.4	25.3	31.5	27.7
Zn	104.3	76.8	111.2	69.5	65.6	86.7	219.6	214.4	190.5	191	16.2	134.4	12.1	87.1	121.3	165.8
Sn	5.2	4.4	1.3	6.1	2.5	11.8	3.4	2.2	1.8	2	9.2	7.4	11.7	10.2	12.1	9.3
Ba	517.5	541.2	488.6	472.4	511.8	470.4	368.54	385.5	389.2	305	288.8	202.1	272.9	202.1	193.6	182.1

Rb	145.1	146.4	129.6	149.2	155.7	153.7	208.5	186.5	176.5	244	236.3	229.1	242.6	249.2	288.9	268.8
Cs	6.7	6.9	3.6	8.9	6.1	7.2	1.1	0.9	2.2	3	13.1	18.7	1.22	6.3	2.6	4.3
Sr	274.4	252.1	238.5	228.3	203.7	217.6	154.5	121.5	168.2	148.2	157.8	149.7	123.1	92.6	74.2	81.4
Ga	24.2	28.6	25.1	27.7	24.8	25.6	29.9	33.5	24.9	28	35.6	39.2	42.7	33.2	36.4	35.5
Nb	16.4	24.9	29.3	27.3	20.9	14.4	46.2	35.1	42.4	26.3	40.4	41.2	42	82.4	69.8	65.6
Zr	148.5	183.1	318.4	398.3	194.6	214.5	376.5	548.9	402.5	466.2	734.4	744.6	807.3	1029.4	985.6	807.1
Y	30.3	41.1	38.5	46.1	36.7	29.6	62.7	53.4	59.7	41	87	75	77	122.6	119.8	112.4
Hf	4.7	4.5	2.7	5.7	3.3	7.2	15.3	11.6	10.9	12.6	11.4	16.6	12.2	28.6	25.3	21.1
Ta	1.4	2	2.3	1.8	1.4	1.1	5.1	3.3	4.01	2.9	3.5	3.4	3.3	7.1	7.3	6.2
Th	10.1	10.8	7.2	13.1	6.6	13.7	17.2	17.7	14.7	15.1	15.9	18.7	15.2	21.8	21.5	26.5
U	2.3	2.5	1.8	2.2	1.9	4.6	6.2	5.4	6.7	3.3	6.2	7.4	6.4	9.5	9.1	10.2
AI	0.95	0.91	0.91	0.93	0.96	0.95	1.03	1.00	1.01	1.00	1.12	1.04	1.01	1.17	1.20	1.15
ASI	0.92	0.96	0.95	0.96	0.93	0.92	0.88	0.91	0.90	0.90	0.80	0.86	0.91	0.79	0.77	0.81
Rb/Zr	0.98	0.80	0.41	0.37	0.80	0.72	0.55	0.34	0.44	0.52	0.32	0.31	0.30	0.24	0.29	0.33
K/Rb	328	318	353	317	313	301	233	234	263	191	206	195	195	187	159	164

Table 1. cont

Sample	Peralkaline granite						Microgranite				Pegmatite							
	PAG-1	PAG-10	PAG-2	PAG-3	PAG-4	PAG-5	Mg1	Mg-2	Mg-3	Mg-4	Peg-1	Peg-11	Peg-13	Peg-16	Peg-18	Peg-4	Peg-6	Peg-8
SiO2	72.09	74.13	71.71	71.65	73.29	71.30	74.49	74.04	74.43	74.68	76.62	73.6	74.59	74.04	73.79	76.78	76.64	76.22
TiO2	0.18	0.16	0.21	0.17	0.21	0.21	0.09	0.16	0.12	0.1	0.31	0.22	0.21	0.11	0.17	0.29	0.31	0.26
Al2O3	13.14	11.36	12.39	12.41	11.92	12.48	11.38	10.57	10.71	11.21	8.5	9.83	10.03	11.14	11.29	7.92	8.06	8.36
Fe2O3	3.42	3.83	2.82	3.11	3.36	3.03	2.95	3.88	4.37	3.56	4.66	5.01	5.07	3.9	3.78	4.72	4.65	4.47
MnO	0.03	0.05	0.05	0.06	0.05	0.05	0.04	0.05	0.06	0.05	0.33	0.09	0.05	0.05	0.04	0.09	0.1	0.15
MgO	0.27	0.17	0.31	0.38	0.22	0.36	0.17	0.1	0.09	0.18	0.15	0.38	0.15	0.14	0.17	0.14	0.13	0.19
CaO	0.56	0.41	0.56	0.63	0.46	0.71	0.26	0.22	0.17	0.34	0.18	0.78	0.31	0.42	0.38	0.18	0.19	0.24
Na2O	6.17	5.33	5.64	6.04	5.58	5.66	4.84	3.69	5.59	4.37	2.74	5.66	5.52	5.63	5.48	2.08	2.94	2.18
K2O	4.48	4.35	4.84	4.66	4.02	4.8	4.58	5.23	3.7	4.01	5.43	3.54	3.28	3.81	4.04	6.11	5.75	6.08
P2O5	0.01	0.03	0.07	0.05	0.03	0.03	0.02	0.02	0.02	0.04	0.04	0.05	0.01	0.02	0.02	0.05	0.05	0.1
LOI	0.755	0.45	0.56	1.06	1.15	0.65	0.69	0.9	0.38	0.79	0.86	0.68	0.38	0.35	0.42	0.76	0.84	1.13
Tot	100	100.	99.	99.	100	99.	99.	99.	100	99.	99.8	99.9	99.	99.	99.	99.	99.	99.3

al	.47	27	99	85	.49	73	66	25	.03	71	2	4	6	61	58	12	66	8
Ni	1.7	3.7	2.6	3.2	3.5	2.4	1.7	2.7	3.6	1.2	7.7	4.2	2.2	1.3	1.1	6.1	7.4	3.4
Co	0.9	2.1	2.3	3.4	2.2	2.6	1	1.3	1.1	1.1	1.5	2	1.4	0.4	0.3	1.4	1.7	1.3
Sc	1.3	1.4	2.4	2.3	1.6	2.4	37.5	23.1	18.9	39.6	27.2	14.3	22.9	36.1	32.4	26.8	39.4	48.7
V	3.1	5.3	16.7	14.3	7.6	18.2	10	14.8	14.5	10.9	31.5	21.5	17.7	15.8	16.4	28.1	26.3	31.7
Cu	5.2	6.7	11.7	12.4	7.6	8.3	9.3	12.3	16.9	6.1	45.7	28.6	31.5	29.7	26.9	38.2	99.1	41.2
Pb	16.2	46.8	23.4	20.1	31.6	25.2	26.6	21.8	30.8	26.1	423.6	258.3	237.2	317.8	224.2	243.5	363.6	361.8
Zn	78.6	53.5	72.2	172.7	74.8	93.6	414.3	240	279.3	259.6	879.6	379.4	508.3	434.4	466.1	597.2	568.6	1024.1
Sn	8.6	18.4	9.1	13.8	17.6	13.4	9	14	22	17.8	96.5	127.2	121.5	94.3	117.8	102.4	89.8	111.6
Ba	74.4	84.8	119.2	92.1	110.4	164.6	106.1	150	19.2	58.5	178.2	236.2	122.9	114.7	124.8	131.1	47.4	158.3
Rb	254.3	311.1	302.2	276.7	306.5	312.8	386	370.3	388.1	391.3	389.7	252.7	306.2	284.5	336.4	356.2	347.3	285.6
Cs	15.9	3.6	5	2.4	4.3	4.9	2.6	3.1	2.3	2.3	29.2	23.5	17.1	28.4	21.9	38.3	76.6	41.7
Sr	30.2	22.8	55.3	41.6	28.8	65.2	24.3	32.9	21.4	34.1	28.6	45.6	10.1	9.4	12.8	26.1	27.9	31.2
Ga	42.3	48.2	31.2	32.5	42.1	35.6	45.2	44.4	45.7	47.3	37.7	48.4	39.4	40.3	44.2	35.8	38.3	42
Nb	84.8	131.5	95.35	98.6	128.6	105.3	203.8	294.1	216.2	194.2	204.2	164.3	135.8	147.1	152.3	157.0	168.6	179.1
Zr	997.2	1226.3	1047.3	915.6	1352.2	1128.8	1677.7	1367.7	2159.7	2252.3	1234.4	1497.5	2396.6	3083.6	2565.3	7727.2	8422.8	1433.7
Y	139.5	241.2	142.5	149.2	199.1	168.7	188.1	314.7	181.7	200.7	223.7	145.8	987.6	828.4	990.3	109.2	118.7	186.2
Hf	27.5	39.5	28.8	30.2	44.5	34.4	35.5	35.9	50.9	60.8	336.4	364.5	130.7	169.6	134.8	221.3	201.4	377.4
Ta	9.6	12.4	10.2	11.9	13.4	9.2	18.2	29.5	17.5	17.1	156.1	95.5	96.7	105.8	95.8	103.7	133.4	140.2
Th	19.3	22	21.6	18.7	27.2	22.7	30.5	50.9	23.9	43.9	430.7	599.7	224.4	243.6	249.7	288.7	368.7	379.7
U	7.8	13.4	9.2	9.3	14.5	10.3	8.7	30.7	26.5	13.7	179.1	141.5	98.8	81.4	98.3	119.8	134.5	156.7
AI	1.14	1.19	1.17	1.21	1.14	1.16	1.14	1.11	1.23	1.03	1.22	1.34	1.26	1.20	1.19	1.27	1.37	1.22
ASI	0.82	0.80	0.80	0.77	0.83	0.79	0.85	0.87	0.79	0.92	0.79	0.67	0.76	0.79	0.80	0.76	0.71	0.79
Rb/Zr	0.26	0.25	0.29	0.30	0.23	0.28	0.23	0.10	0.18	0.16	0.03	0.02	0.13	0.09	0.13	0.05	0.04	0.02
K/Rb	176	140	160	168	131	153	119	141	95	102	139	140	107	134	120	172	166	213

Table 2. Normative compositions for granites of Ad-Dayheen intrusion.

Sample	Monzogranite						Syenogranite				Alkali feldspar granite			Alkaine granite		
	Mon-1	Mon-2	Mon-3	Mon-4	Mon-5	Mon-6	Syen-1	Syen-2	Syen-3	Syen-4	AFG-1	AFG-2	AFG-3	AG-7	AG-8	AG-9
Quartz	23.2	24.47	25.51	25.07	22.59	23.25	21.88	24.35	21.32	23.3	25.67	24.67	24.08	22.91	21.68	26.11
Orthoclase	28.7	28.1	27.5	28.5	29.4	27.9	29.5	28.2	28.0	28.1	29.1	26.9	28.2	28.	27.	26.

	4	5		2	2	4		9	4	4	1	4	7	05	44	52
Albite	39.59	38.32	37.49	38.33	40.48	39.66	41.37	41.19	44.26	41.68	36.05	40.48	40.91	39.21	40.15	38.86
Anorthite	1.72	3.27	3.2	2.79	1.49	2.04	-	0.01	-	0.01	-	-	-	-	-	-
Acmite	-	-	-	-	-	-	1.18	-	0.34	-	1.26	1.29	0.82	1.29	1.38	1.17
Na-Metasilicate	-	-	-	-	-	-	0.09	-	-	-	1.38	0.32	-	2.22	2.71	1.94
Diopside	2.47	1.01	1.43	1	2.35	2.54	3.26	2.85	2.95	3.32	3.87	3.36	2.68	2.57	2.79	2.21
Hypersthene	2.75	3.38	3.39	3.01	2.39	3.06	2.06	2.1	1.97	2.24	2.16	2.59	2.62	3.22	3.31	2.71
Magnetite	0.72	0.67	0.75	0.61	0.6	0.75	-	0.6	0.43	0.7	-	-	0.23	-	-	-
Ilmenite	0.6	0.54	0.6	0.52	0.56	0.62	0.51	0.44	0.48	0.5	[illegible]	0.29	0.33	0.37	0.4	0.37
Apatite	0.18	0.16	0.11	0.13	0.09	0.11	0.13	0.13	0.18	0.09	0.07	0.04	0.04	0.13	0.11	0.09
Colour Index	6.54	5.61	6.17	5.14	5.9	6.98	5.83	6	5.85	6.76	6.44	6.24	5.85	6.15	6.5	5.29
Diff. Index	91.53	90.94	90.5	91.92	92.5	90.85	92.74	93.84	93.62	93.12	90.83	92.08	93.26	90.18	89.27	91.49

Table 2 Cont.

Sample	Peralkaline						Micrographic granite				Pegmatite							
	PAG-1	PAG-10	PAG-2	PAG-3	PAG-4	PAG-5	Mg-1	Mg-2	Mg-3	Mg-4	Peg-1	Peg-11	Peg-13	Peg-16	Peg-18	Peg-4	Peg-6	Peg-8
Quartz	20.88	29.19	23.91	22.9	27.12	22.8	30.93	33.35	31.66	32.07	41.85	31.99	33.46	29.9	29.38	44.41	43.09	42.54
Orthoclase	26.46	25.83	29.08	27.84	24.03	28.21	27.46	31.65	22.11	24.12	32.55	21.19	19.62	22.76	24.15	36.86	34.52	36.71
Albite	42.59	34.36	37.37	38.28	39.[illegible]	38.24	33.49	25.84	34.85	35.94	13.67	31.23	33.72	36.45	35.97	6.84	9.58	9.33
Anorthite	-	-	-	-	-	-	-	-	-	-	-	-	-	-	-	-	-	-
Acmite	1.58	1.76	1.36	1.47	1.59	1.45	1.36	1.82	2	1.49	2.35	2.34	2.34	1.78	1.75	2.26	2.24	2.17
Na-Metasilicate	1.81	2.09	2.23	2.13	1.54	2.09	1.52	0.95	2.49	-	1.67	3.4	2.54	2.25	2.08	1.99	3.06	1.64
Diopside	2.37	1.63	2.04	2.45	1.85	2.92	1.03	0.87	0.64	1.28	0.57	3.13	1.32	1.74	1.56	0.51	0.55	0.48
Hypersthene	3.94	4.75	3.42	3.87	4.04	3.39	3.98	5.15	5.96	4.72	6.65	6.16	6.57	4.84	4.71	6.44	6.23	6.38
Magnetite	-	-	-	-	-	-	-	-	-	0.07	-	-	-	-	-	-	-	-
Ilmenite	0.34	0.31	0.41	0.33	0.4	0.41	0.17	0.31	0.23	0.19	0.6	0.42	0.4	0.21	0.33	0.56	0.6	0.5
Apatite	0.02	0.07	0.16	0.11	0.07	0.07	0.04	0.04	0.04	0.09	0.09	0.11	0.02	0.04	0.04	0.11	0.11	0.22
Colour Index	6.65	6.68	5.87	6.65	6.29	6.72	5.19	6.33	6.83	6.26	7.81	9.72	8.29	6.79	6.6	7.51	7.38	7.37
Diff. Index	89.92	89.39	90.35	89.02	90.5	89.65	91.88	90.85	88.62	92.14	88.07	84.4	86.8	89.11	89.5	88.11	87.19	88.58

Table 3. REE contents of the granitic rocks of Ad-Dayheen intrusion.

	Monzogranite						Syenogranite				Alkali feldspar granite			Alkaline granite		
Sample	Mon-1	Mon-2	Mon-3	Mon-4	Mon-5	Mon-6	Syen-1	Syen-2	Syen-3	Syen-4	AFG-1	AFG-2	AFG-3	AG-7	AG-8	AG-9
La	17.16	21.65	30.22	26.7	40.1	30.34	40.78	29.5	40.74	34.21	42.18	54.45	49.03	50.39	60.68	65.54
Ce	32.78	43.01	67.1	56.85	82.86	62.63	81.56	70.3	83.54	76.54	88.63	105.5	99.1	110.53	128.23	142.73
Pr	3.91	5.43	8.71	7.28	10.02	8.09	9.8	9.75	10.11	9.79	10.65	13.3	12.11	13.46	16.49	18.75
Nd	16.53	20.81	31.5	29.15	37.08	35.5	36.67	41.3	36.72	38.14	40.28	49.15	44.7	51.3	62.92	80.08
Sm	3.83	4.33	5.59	7.09	8.06	8.07	7.42	10.5	7.93	9.39	8.03	9.76	8.27	12.37	15.28	18.76
Eu	0.36	0.41	0.54	0.64	0.69	0.81	0.71	0.72	0.69	0.78	0.81	0.87	0.79	1.01	1.14	1.19
Gd	2.54	3.02	4.1	5.04	6.3	6.31	7.85	8.46	7.28	9	8.68	10.24	11.15	12.72	14.53	16.24
Tb	0.37	0.43	0.58	0.78	0.96	1.01	1.31	1.43	1.14	1.38	1.42	1.63	1.86	2.17	2.39	2.56
Dy	2.32	2.75	3.45	4.49	5.79	5.93	7.5	7.73	7.7	9.25	9.07	10.2	11	13.31	15.45	15.29
Ho	0.48	0.59	0.72	0.92	1.16	1.21	1.6	1.45	1.82	1.88	1.87	2.14	2.37	2.72	3.17	3.24
Er	1.41	1.72	2.11	2.36	3.11	3.34	4.4	3.97	5.48	4.99	5.32	6.01	6.74	7.56	9.09	9.38
Tm	0.21	0.25	0.31	0.36	0.45	0.47	0.68	0.56	0.84	0.77	0.79	0.93	1.01	1.15	1.34	1.4
Yb	1.38	1.64	2.08	2.35	2.93	3.28	4.84	3.8	5.77	5.44	5.19	5.97	6.67	7.55	9.08	9.37
Lu	0.21	0.26	0.33	0.37	0.47	0.5	0.75	0.62	0.9	0.85	0.79	0.91	1.04	1.16	1.35	1.39
∑REE	83.49	106.3	157.34	144.38	199.98	167.49	205.8	190.09	210.66	202.51	224.3	271.06	255.84	287.4	341.14	385.92
Eu/Eu*	0.35	0.35	0.34	0.33	0.36	0.35	0.28	0.23	0.28	0.26	0.32	0.30	0.28	0.25	0.23	0.21
(La/Yb)n	8.41	8.93	9.82	7.68	9.25	6.26	5.70	5.25	4.77	4.25	5.50	6.17	4.97	4.51	4.52	4.73
(La/Sm)n	2.83	3.16	3.41	2.78	3.14	2.37	3.47	1.77	3.24	2.30	3.09	3.52	3.74	2.57	2.51	2.20
(Gd/Lu)n	1.48	1.42	1.52	1.67	1.64	1.55	1.28	1.67	0.99	1.30	1.35	1.38	1.31	1.34	1.32	1.43
(La/Lu)n	8.37	8.53	9.38	7.39	8.74	6.22	5.57	4.88	4.64	4.12	5.47	6.13	4.83	4.45	4.61	4.83

Table 3. Cont.

Sample	Peralkaline granite						Microgranite				Pegmatite							
	PAG-1	PAG-10	PAG-2	PAG-3	PAG-4	PAG-5	Mg-1	Mg-2	Mg-3	Mg-4	Peg-1	Peg-11	Peg-13	Peg-16	Peg-18	Peg-4	Peg-6	Peg-8
La	77.77	100.82	92.5620	73.6416	95.621	84.6219	154.23	234.67	191.17	288.6	660.46	362.71	338.63	399.31	285.72	544.32	491.56	605.69
Ce	1.25	244.09	0.17	1.58	8.06	0.77	332.28	469.2	387.73	590.55	155 1.1	850.22	780.11	937.28	682.56	129 0.97	112 9.61	145 3.04
Pr	22.	34.	25.	20.	28.	24.	44.	60.	55.	74.	198	107	97.	113	81.	158	132	175

	59	49	99	58	76	79	98	07	99	36	.61	.45	22	.99	04	.89	.63	.93
	97.	147	11 1.1	83.	11 5.3	10 0.1	190 .80	230	226	294	750	462	418	482	346	617	534	678
Nd	09	.17	2	93	1	2	3	.33	.17	.2	.51	.09	.69	.45	.59	.73	.06	.9
	22.	32.	26.	20.	28.	24.	46.	47.	58.	72.	211	118	101	115	90.	153	138	173
Sm	71	73	3	16	12	07	32	93	17	55	.42	.03	.38	.9	34	.62	.93	.73
	1.2	1.9	1.5	1.4	1.5	1.6	1.5	1.9	2.3	4.2	11.	6.3	5.4	5.6	4.4		6.9	9.9
Eu	8	4	2	6	7	7	3	9	4	9	03	4	4	6	3	8.2	4	2
	17.	39.	20.	19.	29.	22.	33.	56.	69.	91.	299	140	128	138	116	201	162	231
Gd	96	05	65	71	23	75	43	8	57	54	.68	.39	.44	.05	.09	.81	.98	.92
	2.8	6.0	3.3	3.1	4.8	3.6	5.9	8.4	9.9	13.	55.	26.	24.	23.	20.	39.	30.	45.
Tb	4	8	1	2	3	6	6	7	2	54	68	38	04	51	3	05	34	25
	18.	35.	20.	19.	27.	23.	36.	50.	56.	84.	377	187	160	146	131	250	202	291
Dy	08	01	14	54	69	15	56	05	53	99	.18	.01	.77	.87	.96	.79	.03	.84
	3.8	7.6	4.2	3.8	5.8	4.7	7.2	9.8	11.	17.	82.	39.	35.	33.	27.	53.	43.	62.
Ho	2	6	5	9	4	1	5	1	22	52	64	85	74	82	71	68	85	7
	10.	22.	12.	10.	17.	13.	20.	26.	29.	48.	243	112	1[illegible]	99.	79.	151	125	180
Er	71	5	01	73	01	42	16	4	64	09	.33	.6[illegible]	.[illegible]1	88	01	.19	.88	.24
	1.5	3.3	1.8	1.6	2.5	2.0	2.9	3.7	4.4		36.	17.	1[illegible].	14.	12.	23.	18.	27.
Tm	7	1	6	1	9	8	4	9	9	6.8	1	51	87	92	06	01	92	56
	10.	22.	11.	10.	17.	14.	19.	25.	28.	47.	245	117	102	98.	78.	150	125	179
Yb	54	51	88	91	72	29	7	76	97	47	.6[illegible]	.63	.82	44	35	.46	.31	.5
	1.5	3.3	1.8	1.6	2.7	2.0	2.9	3.8	4.3	6.8	3[illegible]	17.	15.	15.	12.	22.	19.	27.
Lu	9	2	9	2	3	2	3	1	8	2	43	67	76	01	35	96	59	78
			53	43	59	51	899	122	113	164	4[illegible]	256	232	262	196	366	316	
∑R	45	700	3.6	2.4	5.0	2.1	.07	9.0	6.2	1.3	0.8	5.9	7.8	5.0	8.5	6.6	2.6	414
EE	9.8	.68	5	8	6	2	3	8	9	[illegible]	2	1	2	9	1	8	3	4
Eu/ Eu*	0.1 9	0.1 7	0.2 0	0.2 2	0.1 7	0.2 2	0.1 2	0.1 2	0.1 1	0.1 6	0.1 3	0.1 5	0.1 5	0.1 4	0.1 3	0.1 4	0.1 4	0.1 5
(La/ Yb) n	4.9 9	3.0 3	5.2 7	4.5 6	3.6 5	4.0 0	5.2 9	6.1 [illegible]	4.4 6	4.1 1	1.8 2	2.0 9	2.2 3	2.7 4	2.4 7	2.4 5	2.6 5	2.2 8
(La/ Sm) n	2.1 6	1.9 4	2.2 2	2.3 1	2.1 5	2.2 2	2.1 0	3.0 9	2.0 7	2.5 1	1.9 7	1.9 4	2.1 1	2.1 7	2.0 0	2.2 4	2.2 3	2.2 0
(Gd/ Lu) n	1.3 8	1.4 4	1.3 4	1.4 9	1.3 1	1.[illegible] [illegible]	1.4 0	1.8 3	1.9 5	1.6 4	0.9 8	0.9 7	1.0 0	1.1 3	1.1 5	1.0 8	1.0 2	1.0 2
(La/ Lu) n	5.0 1	3.1 1	5.0 2	4.6 6	[illegible] 9	[illegible] 9	5.3 9	6.3 1	4.4 7	4.3 4	1.8 1	2.1 0	2.2 0	2.7 3	2.3 7	2.4 3	2.5 7	2.2 3

Research highlight

- Ad-Dayheen intrusion is a post-collisional rare-metal-bearing A-type granites
- Three pulses of magmatic activity are recognized in the Ad-Dayheen intrusion
- The primary magma was generated by partial melting of the juvenile crust with a minor mantle contribution.
- Ore minerals took place in a magmatic stage followed by a hydrothermal stage
- The pegmatite is highly mineralized with very high concentrations of rare metals and REE

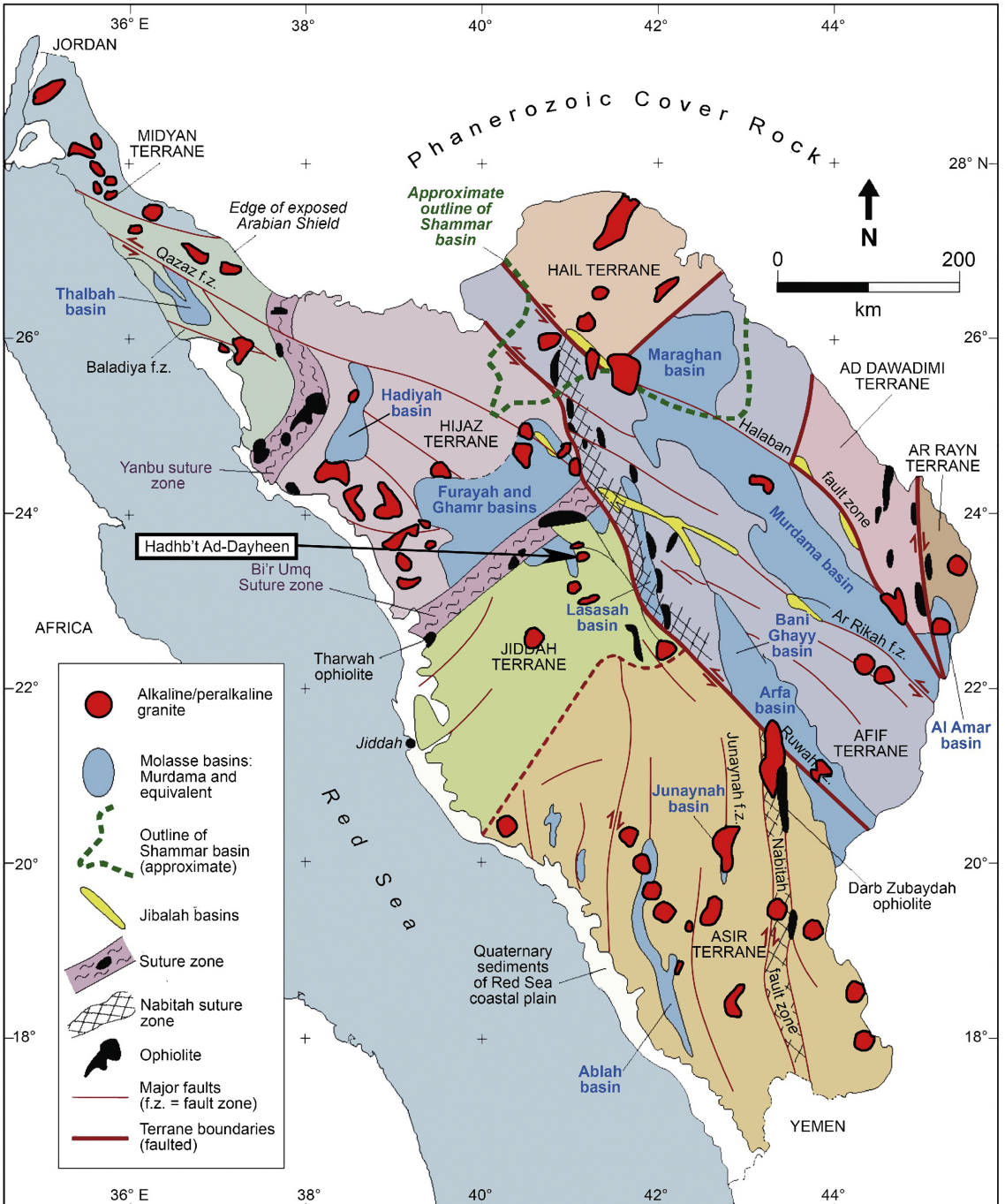
36° E
38°
40°
42°
44°
28° N
26°
24°
22°
20°
18°
JORDAN
MIDYAN TERRANE
Phanerozoic Cover Rock
Edge of exposed Arabian Shield
Approximate outline of Shammar basin
HAIL TERRANE
N
0
200
km
Qazaz f.z.
Thalbah basin
Baladiya f.z.
Maraghan basin
AD DAWADIMI TERRANE
Hadiyah basin
HIJAZ TERRANE
Halaban
fault zone
AR RAYN TERRANE
Yanbu suture zone
Furayah and Ghamr basins
Murdama basin
Hadhb't Ad-Dayheen
Bi'r Umq Suture zone
AFRICA
Lasasah basin
Bani Ghayy basin
Ar Rikah f.z.
Tharwah ophiolite
JIDDAH TERRANE
Arfa basin
Al Amar basin
Jiddah
Ruwah f.z.
AFIF TERRANE
Junaynah f.z.
Junaynah basin
Nabitah f.z.
Darb Zubaydah ophiolite
Red Sea
ASIR TERRANE
Quaternary sediments of Red Sea coastal plain
Ablah basin
YEMEN
Alkaline/peralkaline granite
Molasse basins: Murdama and equivalent
Outline of Shammar basin (approximate)
Jibalah basins
Suture zone
Nabitah suture zone
Ophiolite
Major faults (f.z. = fault zone)
Terrane boundaries (faulted)

Figure 1

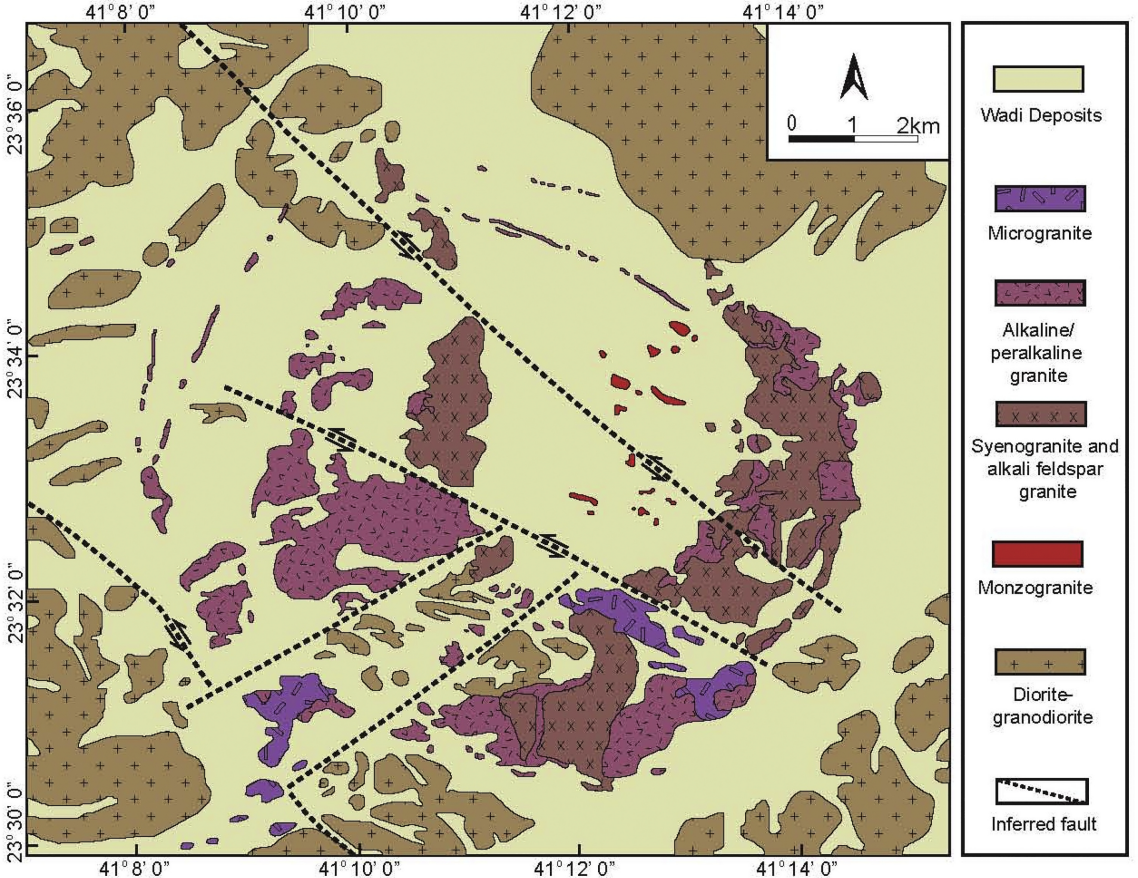
41° 8' 0"
41° 10' 0"
41° 12' 0"
41° 14' 0"
23° 36' 0"
23° 34' 0"
23° 32' 0"
23° 30' 0"
0 1 2km
Wadi Deposits
Microgranite
Alkaline/ peralkaline granite
Syenogranite and alkali feldspar granite
Monzogranite
Diorite-granodiorite
Inferred fault

Figure 2

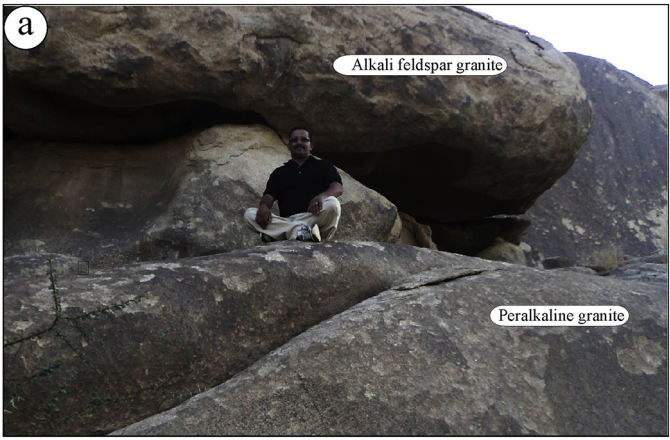
a
Alkali feldspar granite
Peralkaline granite

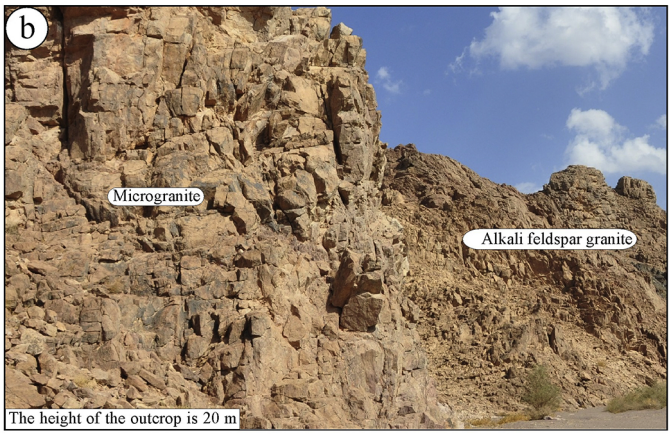
b
Microgranite
Alkali feldspar granite
The height of the outcrop is 20 m

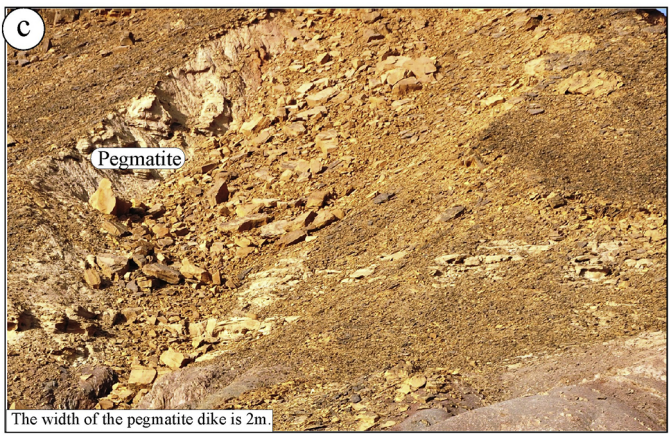
c
Pegmatite
The width of the pegmatite dike is 2m.

Figure 3

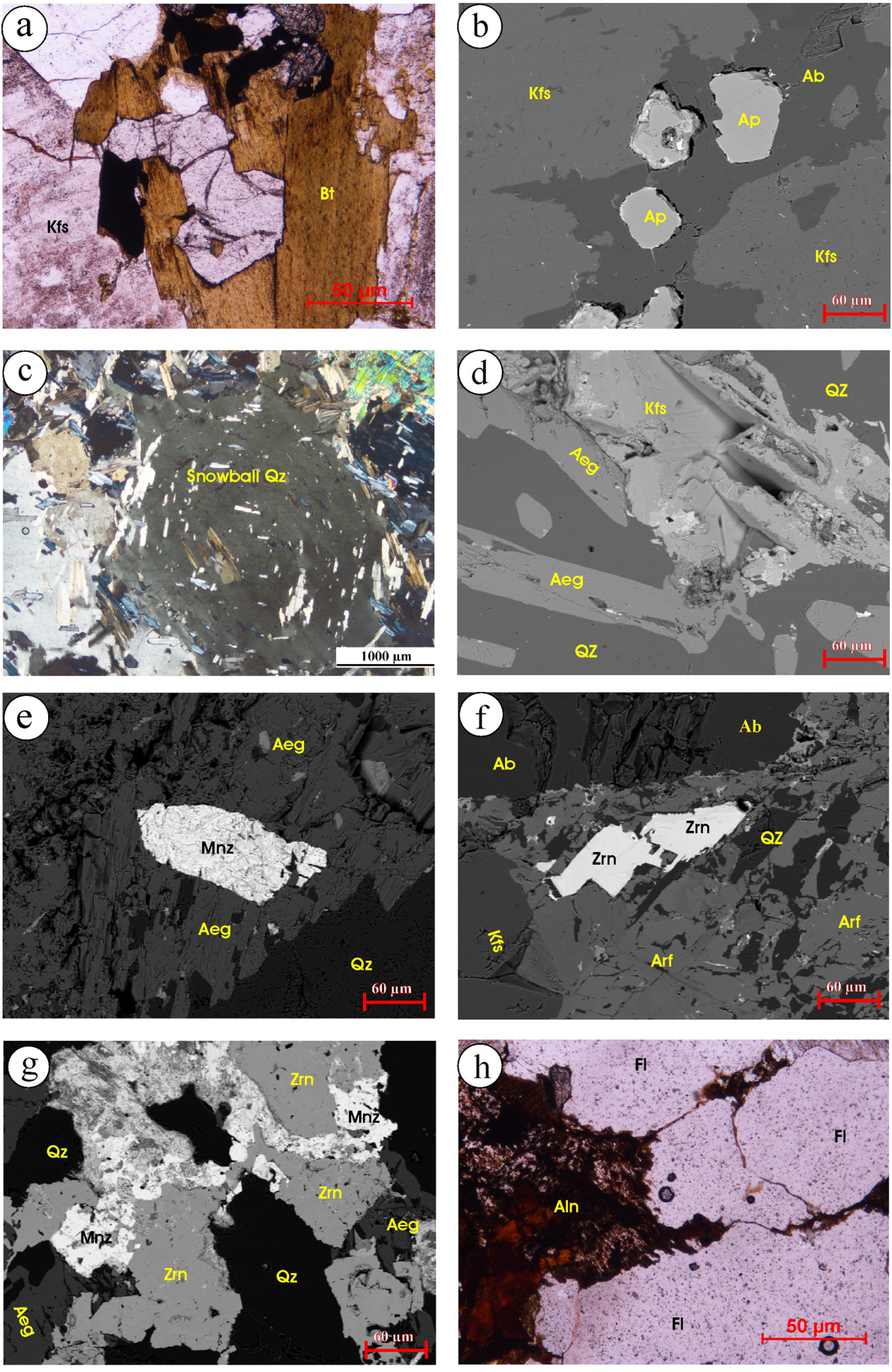
a
Kfs
Bt
50 µm
b
Kfs
Ab
Ap
Ap
Kfs
60 µm
c
Snowball Qz
1000 µm
d
Kfs
QZ
Aeg
Aeg
QZ
60 µm
e
Aeg
Mnz
Aeg
Qz
60 µm
f
Ab
Ab
Zrn
Zrn
QZ
Kfs
Arf
Arf
60 µm
g
Zrn
Mnz
Qz
Zrn
Aeg
Mnz
Zrn
Qz
Aeg
60 µm
h
Fl
Fl
Aln
Fl
50 µm

Figure 4a

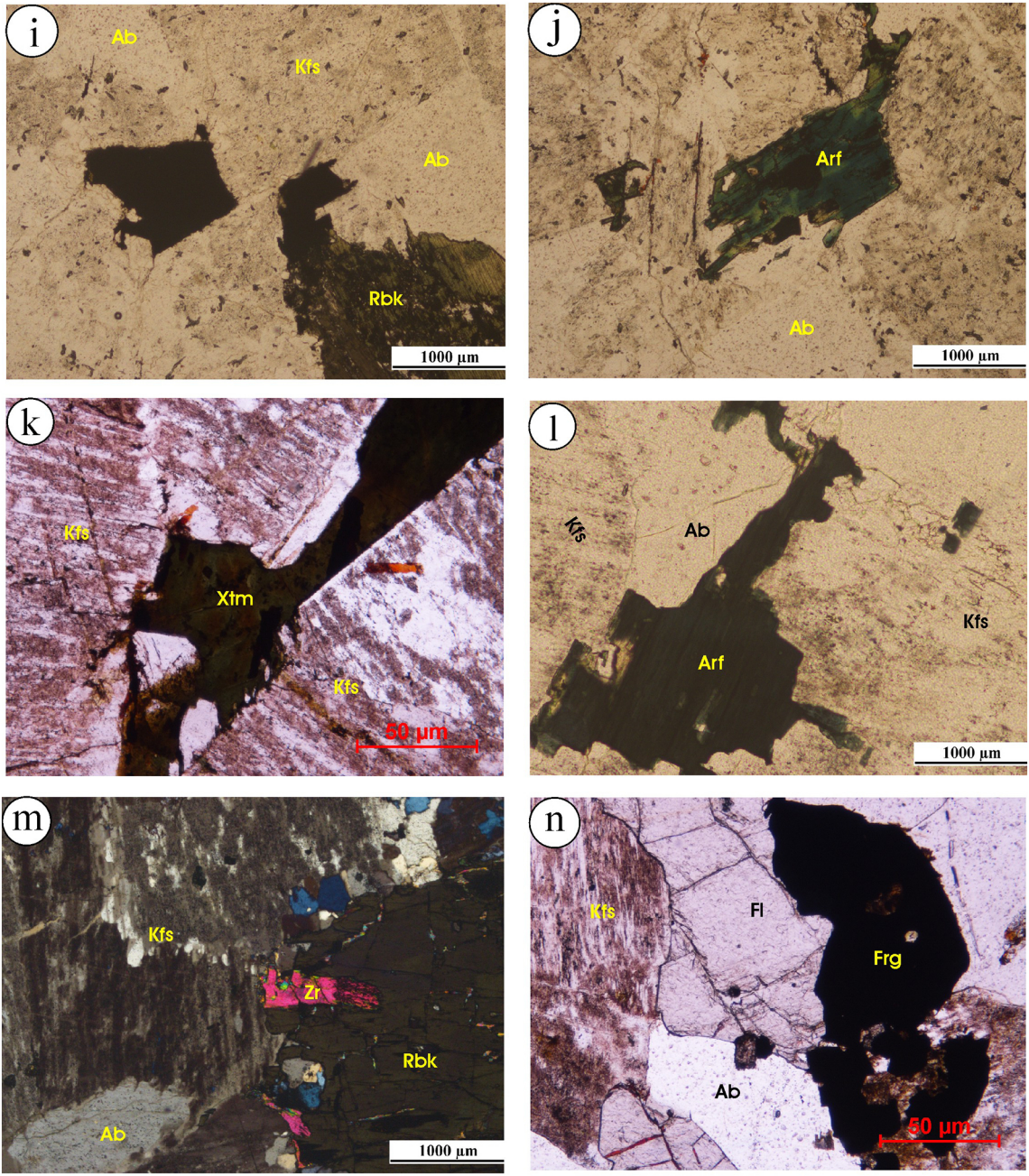
i
Ab
Kfs
Ab
Rbk
1000 µm
j
Arf
Ab
1000 µm
k
Kfs
Xtm
Kfs
50 µm
l
Kfs
Ab
Kfs
Arf
1000 µm
m
Kfs
Zr
Rbk
Ab
1000 µm
n
Kfs
Fl
Frg
Ab
50 µm

Figure 4b

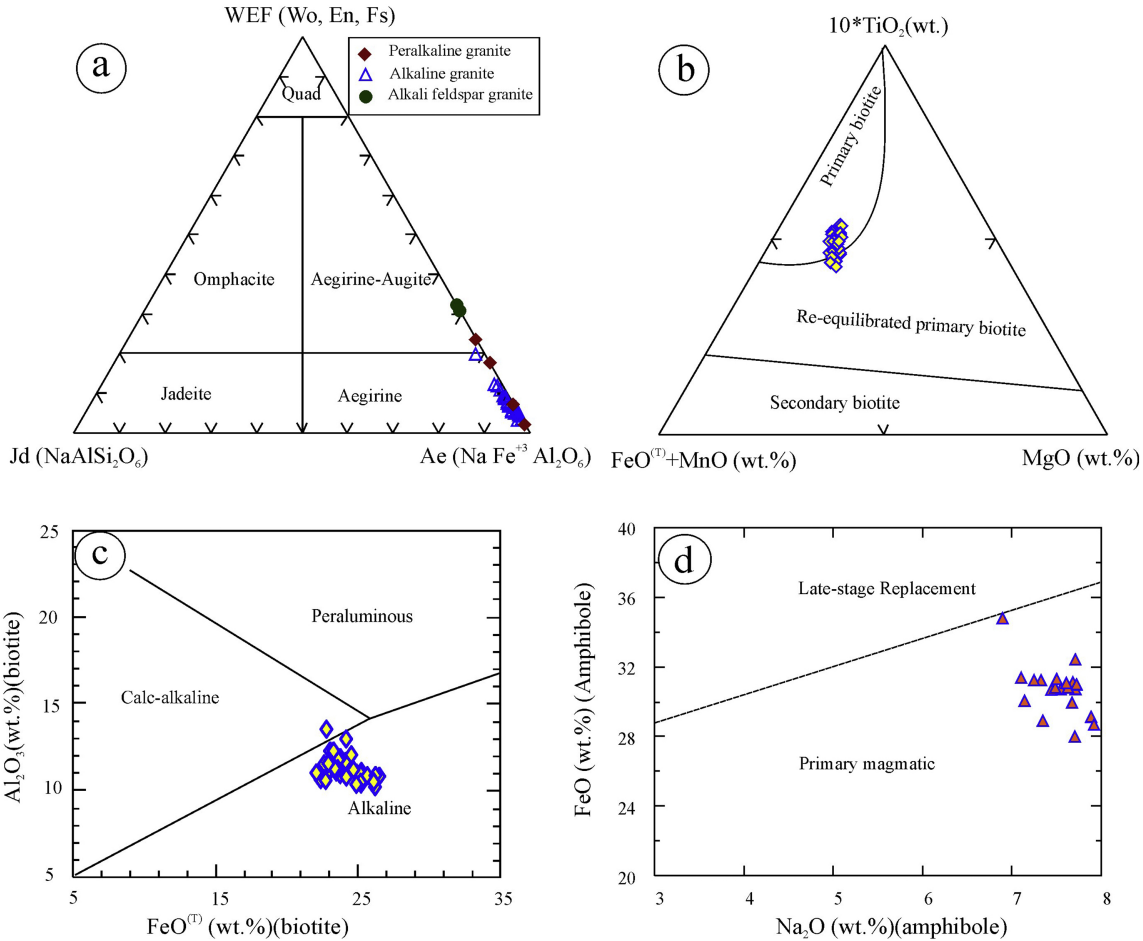
a
WEF (Wo, En, Fs)
Peralkaline granite
Alkaline granite
Alkali feldspar granite
Quad
Omphacite
Aegirine-Augite
Jadeite
Aegirine
Jd (NaAlSi2O6)
Ae (Na Fe+3 Al2O6)
b
10*TiO2(wt.)
Primary biotite
Re-equilibrated primary biotite
Secondary biotite
FeO(T)+MnO (wt.%)
MgO (wt.%)
c
Peraluminous
Calc-alkaline
Alkaline
Al2O3(wt.%)(biotite)
FeO(T) (wt.%)(biotite)
d
Late-stage Replacement
Primary magmatic
FeO (wt.%) (Amphibole)
Na2O (wt.%)(amphibole)

Figure 5

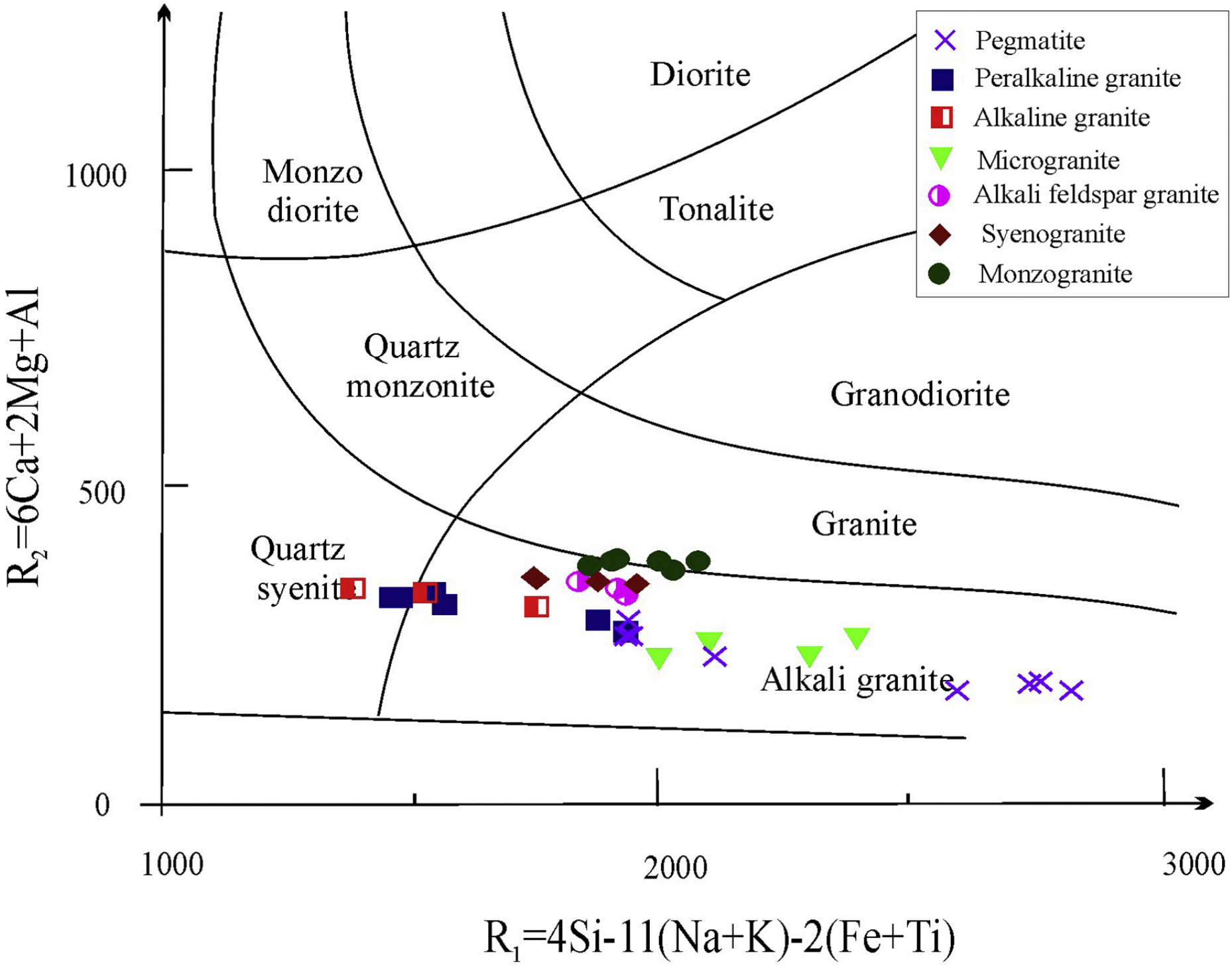
Pegmatite
Peralkaline granite
Alkaline granite
Microgranite
Alkali feldspar granite
Syenogranite
Monzogranite
Diorite
Monzo diorite
Tonalite
Quartz monzonite
Granodiorite
Granite
Quartz syenite
Alkali granite
1000
500
0
1000
2000
3000
R2=6Ca+2Mg+Al
R1=4Si-11(Na+K)-2(Fe+Ti)

Figure 6

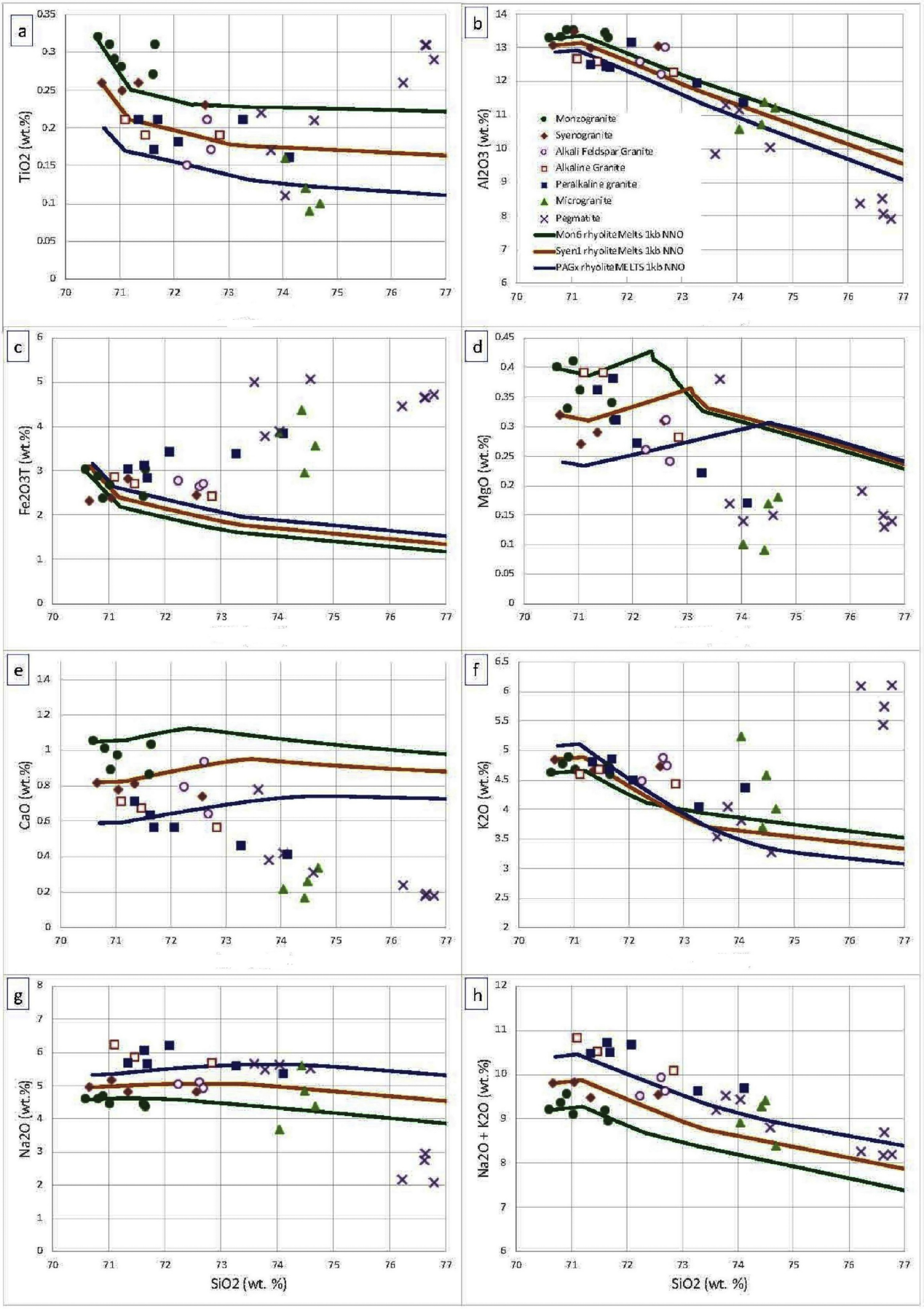
a
TiO2 (wt.%)
b
Al2O3 (wt.%)
Monzogranite
Syenogranite
Alkali Feldspar Granite
Alkaline Granite
Peralkaline granite
Microgranite
Pegmatite
Mon6 rhyolite MELTS 1kb NNO
Syen1 rhyolite MELTS 1kb NNO
PAGx rhyolite MELTS 1kb NNO
c
Fe2O3T (wt.%)
d
MgO (wt.%)
e
CaO (wt.%)
f
K2O (wt.%)
g
Na2O (wt.%)
SiO2 (wt. %)
h
Na2O + K2O (wt.%)
SiO2 (wt. %)

Figure 7

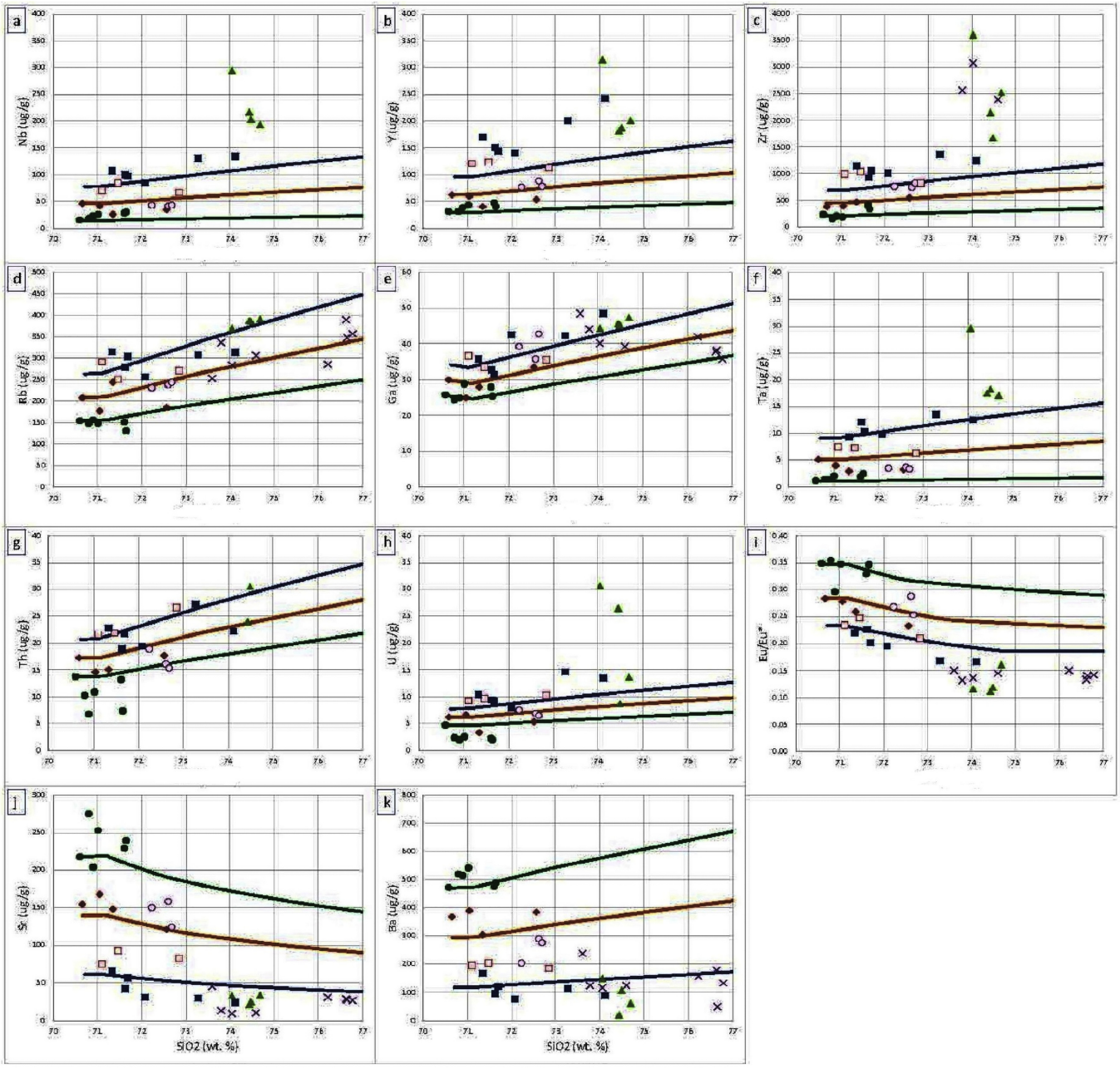
a
Nb (ug/g)
b
Y (ug/g)
c
Zr (ug/g)
d
Rb (ug/g)
e
Ga (ug/g)
f
Ta (ug/g)
g
Th (ug/g)
h
U (ug/g)
i
Eu/Eu*
j
Sr (ug/g)
SiO2 (wt. %)
k
Ba (ug/g)
SiO2 (wt. %)

Figure 8

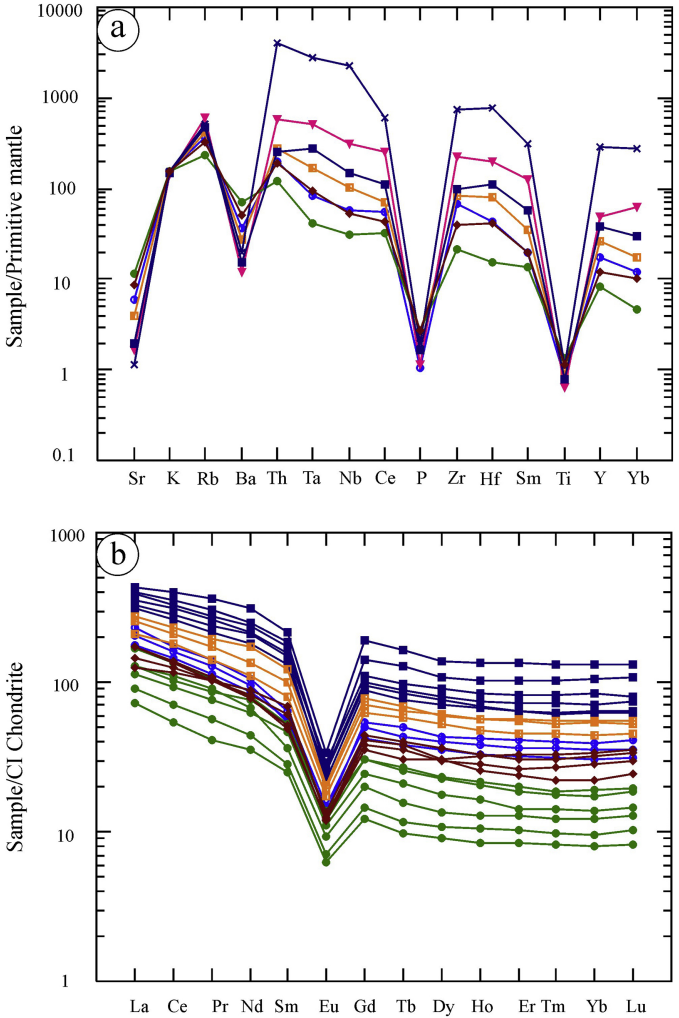
a
Sample/Primitive mantle
10000
1000
100
10
1
0.1
Sr K Rb Ba Th Ta Nb Ce P Zr Hf Sm Ti Y Yb
b
Sample/CI Chondrite
1000
100
10
1
La Ce Pr Nd Sm Eu Gd Tb Dy Ho Er Tm Yb Lu

Figure 9

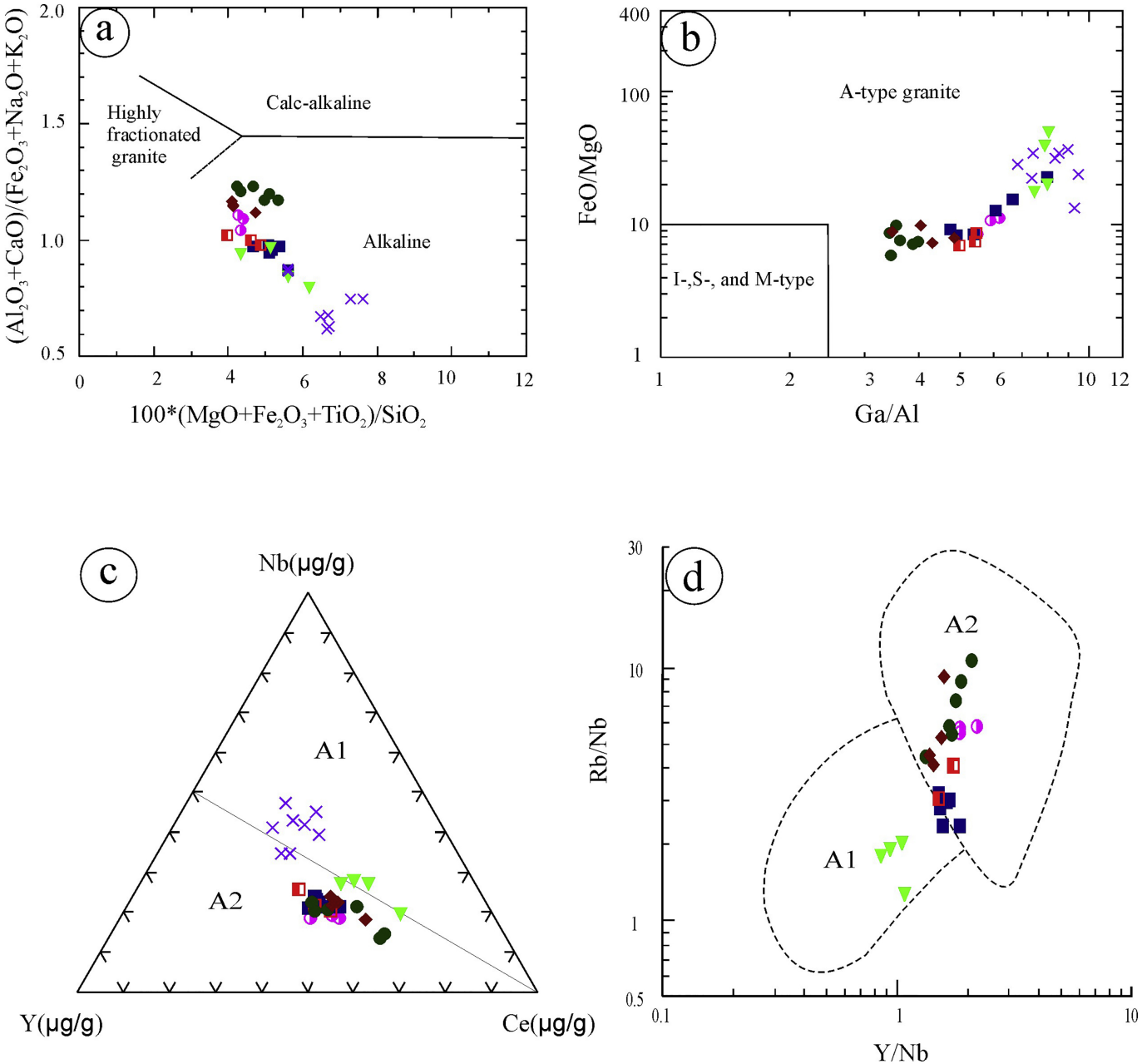
a
Calc-alkaline
Highly fractionated granite
Alkaline
(Al2O3+CaO)/(Fe2O3+Na2O+K2O)
100*(MgO+Fe2O3+TiO2)/SiO2
b
A-type granite
I-,S-, and M-type
FeO/MgO
Ga/Al
c
Nb(μg/g)
A1
A2
Y(μg/g)
Ce(μg/g)
d
A2
A1
Rb/Nb
Y/Nb

Figure 10

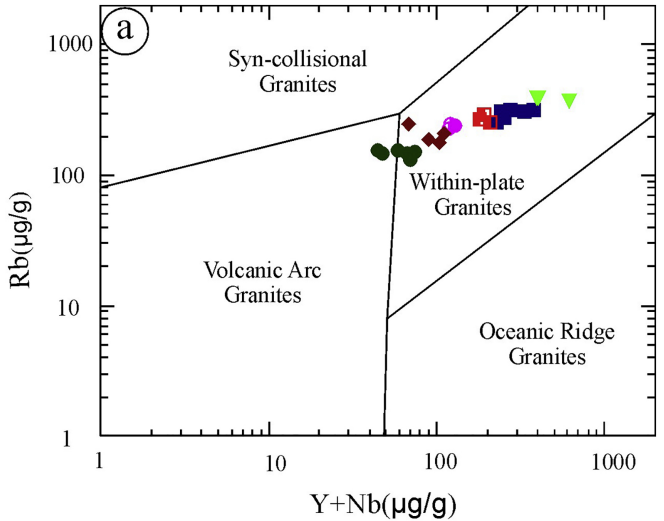
a
Syn-collisional
Granites
Within-plate
Granites
Volcanic Arc
Granites
Oceanic Ridge
Granites
Rb(μg/g)
Y+Nb(μg/g)
1000
100
10
1
1
10
100
1000

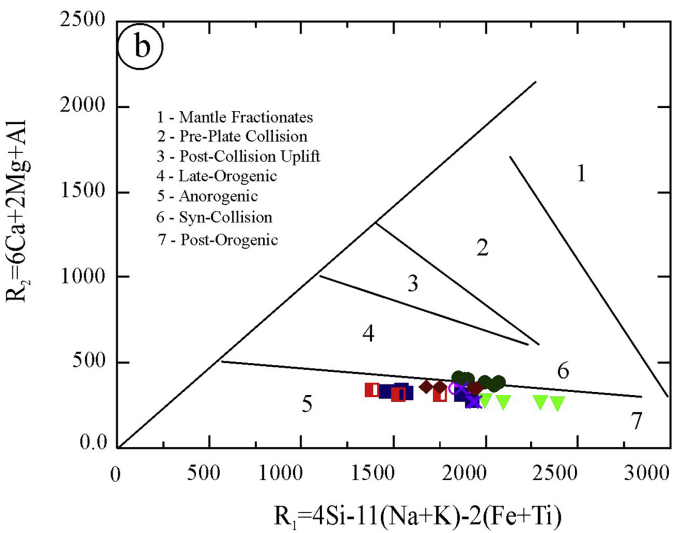
b
1 - Mantle Fractionates
2 - Pre-Plate Collision
3 - Post-Collision Uplift
4 - Late-Orogenic
5 - Anorogenic
6 - Syn-Collision
7 - Post-Orogenic
R2=6Ca+2Mg+Al
R1=4Si-11(Na+K)-2(Fe+Ti)
2500
2000
1500
1000
500
0.0
0
500
1000
1500
2000
2500
3000

Figure 11

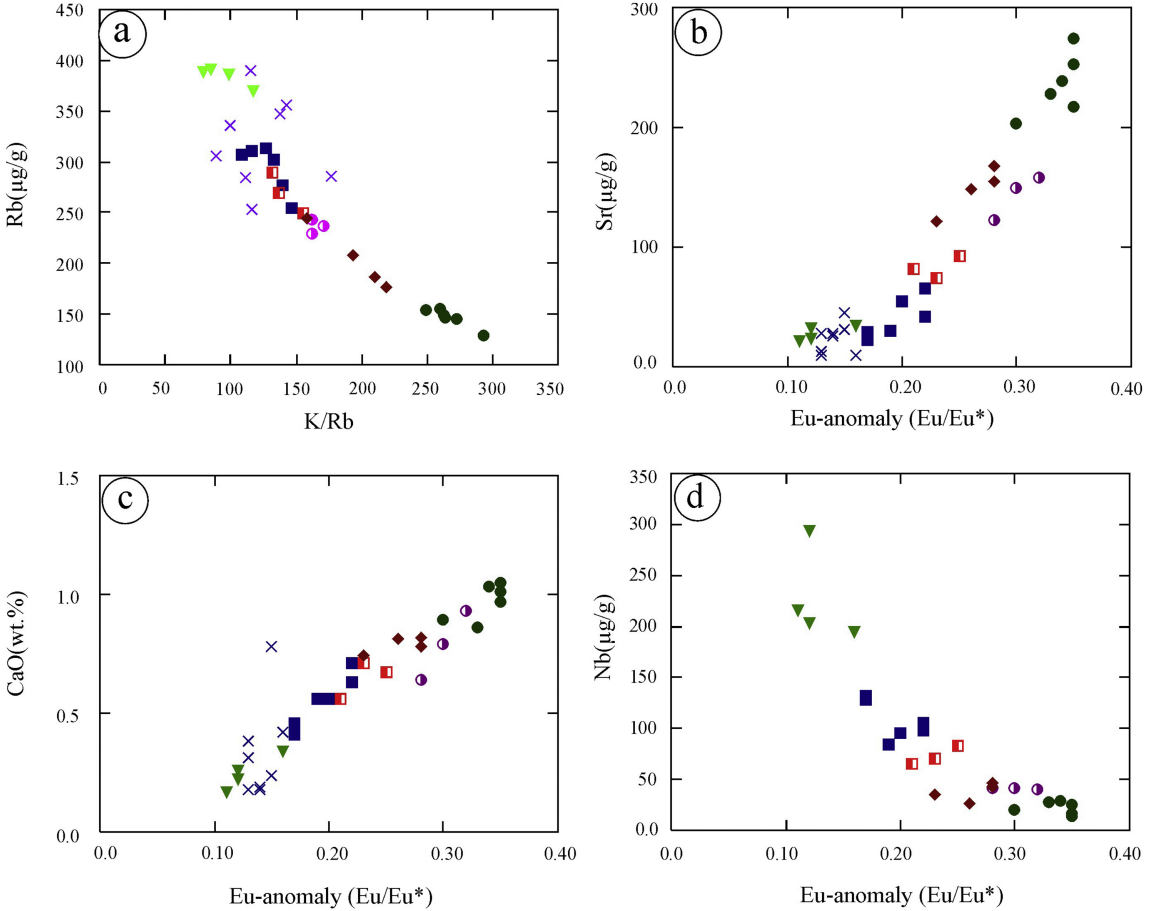
a
Rb(µg/g)
K/Rb
b
Sr(µg/g)
Eu-anomaly (Eu/Eu*)
c
CaO(wt.%)
Eu-anomaly (Eu/Eu*)
d
Nb(µg/g)
Eu-anomaly (Eu/Eu*)

Figure 12

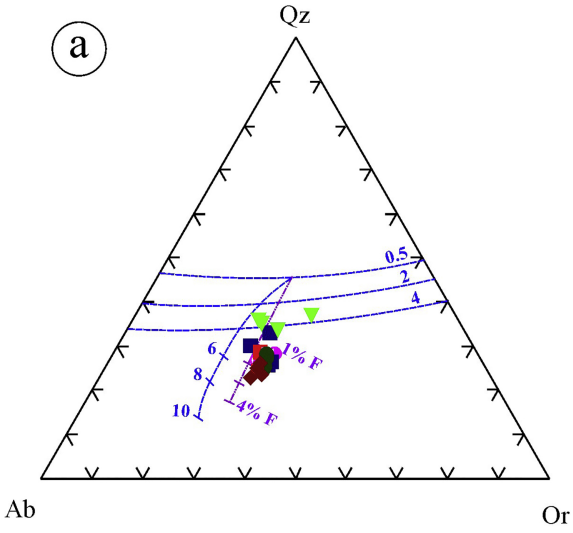
a
Qz
Ab
Or
0.5
2
4
6
8
10
1% F
4% F

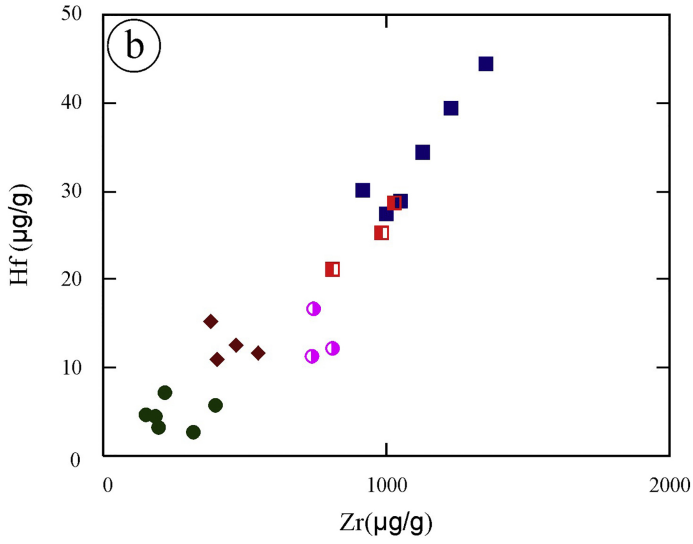
b
Hf (µg/g)
Zr(µg/g)
0
10
20
30
40
50
0
1000
2000

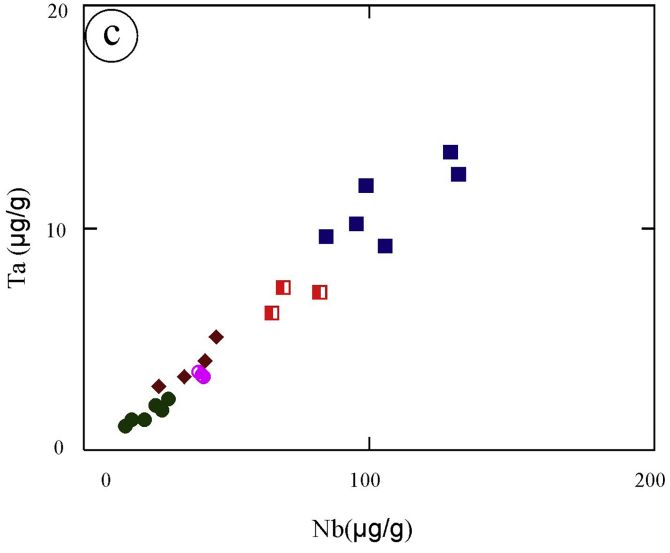
c
Ta (µg/g)
Nb(µg/g)
0
10
20
0
100
200

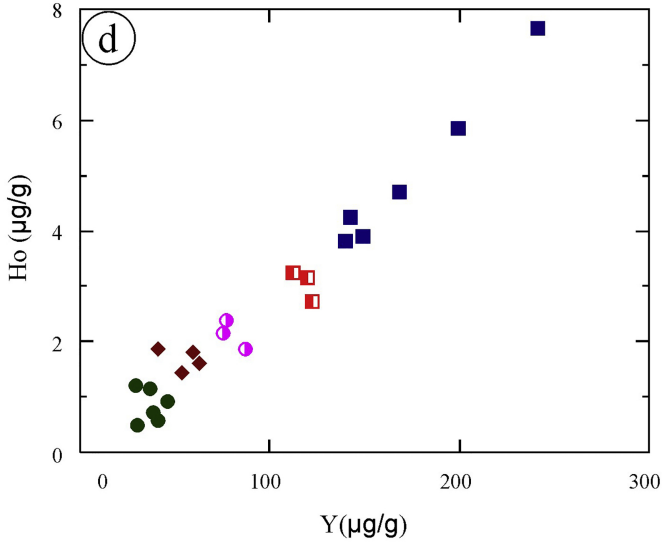
d
Ho (µg/g)
Y(µg/g)
0
2
4
6
8
0
100
200
300

Figure 13